JETP Letters, Vol. 76, No. 12, 2002, pp. 693–696. Translated from Pis'ma v Zhurnal Éksperimental'noĭ i Teoreticheskoĭ Fiziki, Vol. 76, No. 12, 2002, pp. 821–824.

Measurement of the Magnetic Moment of a Negative Muon in Zinc and Cadmium

T. N. Mamedov[1, *], A. S. Baturin[2], D. Herlach[3], O. D. Maslov[1], A. V. Stoĭkov[1], and U. Zimmermann[3]

[1] *Joint Institute for Nuclear Research, Dubna, Moscow region, 141980 Russia*
**e-mail: tmamedov@nu.jinr.ru*
[2] *Moscow Institute of Physics and Technology, Institutskiĭ per. 9, Dolgoprudnyĭ, Moscow region, 141700 Russia*
[3] *Paul Scherrer Institut, CH-5232 Villigen PSI, Switzerland*

Received October 29, 2002

The magnetic moment (g factor) of a negative muon on the 1s atomic levels of zinc and cadmium was measured with an accuracy higher by a factor of 7 than the accuracy achieved in other measurements. The experimental value of the g factor differs substantially from the theoretical results. Possible causes of this discrepancy are discussed. © *2002 MAIK "Nauka/Interperiodica".*

PACS numbers: 14.60.Ef; 13.40.Em; 31.30.Jv; 36.10.Dr; 76.75.+i

Measurement of the magnetic moment of a negative muon on the 1s atomic level is of interest as a check of the predictions made (i) by quantum theory for particles with spin 1/2, according to which the magnetic moment of a particle bound in an atom must differ from the magnetic moment of a free particle because of the relativistic motion and (ii) by QED about the additional (compared to a free particle) radiative corrections to the magnetic moment because of the Coulomb field of the nucleus. The additional radiative corrections are two orders of magnitude smaller than the correction due to the relativistic motion of the particle.

The g factor of a negative muon on the 1s level of an atom with zero spin of the nucleus and electron shell is expressed as [1]

$$(g_\mu^{1s}) = 2\left(1 + \sum_{i=1}^{7} a_\mu^{(i)}\right), \qquad (1)$$

where $a_\mu^{(1)}$ are the radiative corrections for a free muon, $a_\mu^{(2)}$ are the additional radiative corrections arising in the Coulomb field of a nucleus, $a_\mu^{(3)}$ is the relativistic correction, $a_\mu^{(4)}$ is the correction for nuclear polarization, $a_\mu^{(5)}$ is the correction for the polarization of the atomic electron shell in an external magnetic field (and for the polarization of free charge carriers), $a_\mu^{(6)}$ is the correction for the diamagnetic shielding of an external magnetic field by the atomic electron shell, and $a_\mu^{(7)}$ is the correction for the center of mass of the nucleus + muon system.

Strictly speaking, $a_\mu^{(5)}$ and $a_\mu^{(6)}$ are not corrections to the muon magnetic moment but determine the difference between the magnetic field on a muon and the external magnetic field. These corrections arise because the negative muon is inside the electron shell of an atom, which, in turn, interacts with other atoms and free charge carriers.

Ford *et al.* [1] numerically calculated the quantity $(g_\mu^{\text{free}} - g_\mu^{1s})/g_\mu^{\text{free}}$ for a number of atoms, where $g_\mu^{\text{free}} = 2(1 + a_\mu^{(1)})$ is the g factor of a free muon ($a_\mu^{(1)} = 0.0011659230(84)$ [2]). The $a_\mu^{(5)}$ correction was ignored in [1]. Values accepted for $a_\mu^{(6)}$ in [1] for atoms with $Z \lesssim 50$ are close to those calculated later [3] in relativistic Hartree–Fock–Slater theory. Recently, Karshenboim *et al.* [4] obtained an analytic expression for the $a_\mu^{(2)}$ and $a_\mu^{(3)}$ corrections, which applies in a limited range of the nuclear charge Z.

Corrections to the g factor of an electron on the 1s atomic level are similar to the above-mentioned corrections for a muon, except for $a_\mu^{(5)}$ and $a_\mu^{(6)}$, because measurements for the 1s electron are carried out in hydrogen-like ions (with one 1s electron).

At present, g_e^{1s} has been measured in hydrogen [5], deuterium [6], helium [7], and carbon [8, 9]. These measurements are consistent with theoretical calculations [10, 11] to within errors. However, only in carbon does experimental accuracy make it possible to verify QED predictions for radiative corrections to the magnetic moment of the 1s electron.

0021-3640/02/7612-0693$22.00

Measurement of the magnetic moment of a bound muon is of special interest, because the Coulomb field for the negative muon on the 1*s* atomic level is much stronger than for the 1*s* electron. In particular, the Coulomb field for a muon in carbon is comparable with the field for the 1*s* electron in lead.

The magnetic moment of a negative muon on the 1*s* atomic level was measured in carbon, oxygen, magnesium, sulfur, zinc, cadmium, and lead [12–16] (The quantity $(g_\mu^{\text{free}} - g_\mu^{1s})$ in zinc, cadmium, and lead was measured with an accuracy of ~50% [14]). The measured and calculated values of the muon *g* factor disagree in some cases. In [16], the discrepancy for oxygen and magnesium was attributed to the $a_\mu^{(5)}$ correction, which was ignored in [1]. The quantity g_μ^{1s} for zinc, which was obtained in [16], where $(g_\mu^{\text{free}} - g_\mu^{1s})$ was measured with an accuracy higher than in [14] by a factor of 3, differs from the theoretical value.

The aim of this work is to improve the accuracy of measurement of the *g* factor of a muon on the 1*s* atomic levels of zinc and cadmium. Measurements in carbon and silicon are also repeated.

Measurements were carried out at the GPD setup [17] placed on a muon beam from the μE1 channel of the PSI accelerator (Paul Scherrer Institute, Switzerland). A magnetic field of 4100 G in a sample was produced by Helmholtz coils. The magnetic field was perpendicular to the axis of the muon beam. The long-term stability of the current in Helmholtz coils was close to 2×10^{-5}. The Earth's magnetic field and fields from magnetic materials placed near the setup were compensated to an accuracy of 0.01 G. Carbon, silicon, zinc, and cadmium disc samples were 30 mm in diameter and 12, 10, 7, and 3 (6×0.5) mm in thickness, respectively. They were placed at the center of Helmholtz coils, whose positions were corrected so that the axis of the beam curved in the magnetic field passed through the center of a sample. The positions of the samples with respect to the beam axis and center of Helmholtz coils were fixed with an accuracy of ~1 mm.

By X-ray fluorescence analysis (with a cadmium source), we determined that the contents of Fe, Co, Ni, and Cu in the zinc samples were 0.5, 0.5, 0.1, and 0.3 at. %, respectively. Analysis by a scanning electron microscope with an X-ray microanalyzer (JEOL-840) and electron energy of 25 keV showed the following contents of impurities: (i) 0.1–0.2 at. % of Cu and less than 0.2 at. % of Al, Ca, Sc, Ti, V, Cr, Mn, Fe, Co, Ni, Ga, and Ge in the zinc samples; (ii) less than 0.1 at. % of Fe and less than 0.2 at. % of Ca, Sc, Ti, V, Cr, Mn, Co, Ni, Zn, Ga, Ge, Rb, Sr, Y, Zr, Nb, Mo, Tc, Ru, Rh, Pd, Ag, In, Sn, Sb, and Te in the cadmium samples.

In order to increase the rate of data accumulation, decay electrons were detected by four telescopes of scintillation counters, in contrast to the preceding measurement [16]. Two telescopes, which were absent in the measurements reported in [16], were placed upwards and downwards from the target (up and down telescopes) so that the muon beam did not directly intersect them.

The muon *g* factor was determined from the precession frequency ω of the muon spin in an external magnetic field:

$$(g_\mu^{\text{free}} - g_\mu^{1s})/g_\mu^{\text{free}} = (\omega^{\text{free}} - \omega)/\omega^{\text{free}},$$

where ω^{free} and g_μ^{free} are the spin precession frequency and *g* factor of a free muon, respectively. The frequency ω^{free} was determined experimentally from the precession frequency of a positive muon in copper. The procedure of measuring and processing experimental data was reported in detail in [16]. During measurement, the stability of the setup parameters was monitored by determining the frequency of the periodic background structure in the μSR spectra (background structure was determined by the rf field of the accelerator) and was no worse than 10^{-5}.

The table presents available experimental data on the muon *g* factor on the 1*s* levels of various atoms, including our measurements and theoretical calculations. The accuracy of our measurements for zinc and silicon is seven times higher than in [14]. Different measurements for carbon and cadmium coincide with each other.

Experimental data confirm that $(g_\mu^{\text{free}} - g_\mu^{1s})/g_\mu^{\text{free}}$ increases with the nuclear charge *Z*. Nevertheless, the table demonstrates that the measured values of $(g_\mu^{\text{free}} - g_\mu^{1s})/g_\mu^{\text{free}}$ are smaller than the values calculated for almost all samples. For light elements (including sulfur), this difference is no greater than 7×10^{-4}, which can be attributed to the fact that the effects associated with the polarization of the electron shell of a muonic atom and conduction electrons were ignored in theoretical calculations (see [16]).

We recall that the electron shells of the muonic atoms formed as a result of the capture of a negative muon by the Zn and Cd atoms are completely similar to the electron shells of the Cu and Ag atoms, respectively. For this reason, to correctly compare our data with theoretical calculations [1], the Knight shift in the Cu and Ag atoms in the Cu–Zn and Ag–Cd alloys, respectively, must be taken into account. In addition, it is necessary to take into account that a sample (metallic zinc or cadmium) contains no more than one muonic atom at any time under the conditions of the experiment.

Cu–Zn and Ag–Cd alloys are extensively used in engineering, and the Knight shifts for Cu and Ag in Cu–Zn and Ag–Cd alloys, respectively, are well studied (see [18–21]). As follows from the NMR data [18], the Cu Knight shift in the $Cu_{1-x}Zn_x$ alloy decreases from 0.235 to (0.15 ± 0.01)% as *x* increases from 0 to 39%

Experimental data and theoretical calculations of the g factor of a negative muon in carbon, oxygen (water), magnesium, silicon, sulfur, zinc, cadmium, and lead

Sample	$10^4 \times (g_\mu^{\text{free}} - g_\mu^{1s})/g_\mu^{\text{free}}$				
	this work	experiment [15, 16]	experiment [12]	experiment [14]	theory [1]
C (graphite)	7.5 ± 0.2	7.9 ± 0.7	7.6 ± 0.3		8.2 ± 0.1
			7.1 ± 0.6		
			8.0 ± 0.5		
O in H_2O		7.0 ± 1.1	9.4 ± 1.0		14.3 ± 0.2
Mg metallic		23.1 ± 0.9	26.4 ± 0.7		29.8 ± 0.6
Mg in MgH_2			29.6 ± 0.7		
Si crystal	36 ± 2	35.9 ± 1.1	36.3 ± 1.1		39.1 ± 1.0
S amorphous		42.4 ± 2.1	48.2 ± 1.6		49.1 ± 1.5
Zn	75 ± 9	77 ± 22		120 ± 62	129 (≥122)
Cd*	67 ± 22			201 ± 140	218 (≥175)
Pb				468 ± 220	383

*Theoretical values of the $a_\mu^{(2)}$ and $a_\mu^{(4)}$ corrections for cadmium were obtained by interpolating data from [1], and the $a_\mu^{(6)}$ correction was taken from [3].

(α phase). The Cu Knight shift is equal to (0.15 ± 0.01)% and (0.07 ± 0.01)% for 40% ≤ x ≤ 57% (β phase) and 57% ≤ x ≤ 68% (γ phase), respectively. Therefore, a value of $(7 \pm 1) \times 10^{-4}$ can be treated as the upper limit of the $_\mu$Cu Knight shift in zinc. The concentration dependence of the Ag Knight shift in the Ag–Cd alloy [19, 21] indicates that the Knight shift for the $_\mu$Ag atom in Cd does not exceed $(42.9 \pm 0.4) \times 10^{-4}$. In brackets, the last column of the table presents the quantity $(g_\mu^{\text{free}} - g_\mu^{1s})/g_\mu^{\text{free}}$ calculated with the inclusion of the Knight shift. Obviously, the inclusion of the Knight shift does not eliminate the discrepancy (on the order of five standard errors) between calculations and experimental data for Zn and Cd.

Experiments [22–24] devoted to the effect of transition atomic impurities (Cr, Mn, Fe, Co, Ni) on the Knight shift for the nuclei of matrix atoms in various alloys indicate that impurities in the samples (Zn and Cd) that we examined can change the Knight shift by no more than 10% ($\Delta\mathcal{K}/\mathcal{K} \lesssim 0.1$) compared to the pure samples.

The corrections $a_\mu^{(2)}$, $a_\mu^{(4)}$, and $a_\mu^{(7)}$ are small, and the inaccuracy of their calculation is unlikely to be responsible for the observed discrepancies for Zn and Cd. The correction $a_\mu^{(1)}$ is known to a high accuracy from independent experiments. The diamagnetic correction $a_\mu^{(6)}$ was well calculated (see, e.g., [3]), and the results do not differ significantly from the experimental data on atomic magnetic susceptibility. Therefore, either the Knight shift on a muonic atom is anomalous in zinc and cadmium or the calculation [1] of the relativistic correction $a_\mu^{(3)}$ is inaccurate. The anomalous Knight shift in a muonic atom was observed, in particular, in paramagnetic MnO [25].

Thus, experimental values of the g factor of a negative muon on the 1s level of the Zn and Cd atoms differ significantly (by five standard errors) from calculations. This discrepancy can testify both to the anomalous Knight shift for a muonic atom in zinc and cadmium and to the inaccuracy of the calculated relativistic correction to the muon magnetic moment. We expect that measurement of g_μ^{1s} in crystalline germanium (which is a diamagnetic substance, where the Knight shift is negligible) will make it possible to determine the causes of discrepancies.

We are grateful to the management of the Paul Scherrer Institute, where these measurements were carried out. This work was supported by the Ministry of Education of the Russian Federation, program "Universities of Russia," project no. 01.01.015.

REFERENCES

1. K. W. Ford and J. G. Wills, Nucl. Phys. **35**, 295 (1962); K. W. Ford, V. W. Hughes, and J. G. Wills, Phys. Rev. **129**, 194 (1963).
2. Particle Data Group, Eur. Phys. J. C **3**, 1 (1998).
3. F. D. Feiock and W. R. Johnson, Phys. Rev. **187**, 39 (1969).
4. S. G. Karshenboim, V. G. Ivanov, and V. M. Shabaev, Zh. Éksp. Teor. Fiz. **120**, 546 (2001) [JETP **93**, 477 (2001)].
5. J. S. Tiedeman and H. G. Robinson, Phys. Rev. Lett. **39**, 602 (1977).

6. F. G. Walther, W. D. Phillips, and D. Kleppner, Phys. Rev. Lett. **28**, 1159 (1972).
7. C. E. Johnson and H. G. Robinson, Phys. Rev. Lett. **45**, 250 (1980).
8. N. Hermanspahn, H. Häffner, H.-J. Kluge, *et al.*, Phys. Rev. Lett. **84**, 427 (2000).
9. H. Häffner, T. Beier, N. Hermanspahn, *et al.*, Phys. Rev. Lett. **85**, 5308 (2000).
10. H. Persson, S. Salomonson, P. Sunnergren, and I. Lindgren, Phys. Rev. A **56**, R2499 (1997).
11. H. Grotch and R. A. Hegstrom, Phys. Rev. A **4**, 59 (1971).
12. D. P. Hutchinson, J. Menes, G. Shapiro, and A. M. Patlach, Phys. Rev. **131**, 1362 (1963).
13. J. H. Brewer, Hyperfine Interact. **17–19**, 873 (1984).
14. T. Yamazaki, S. Nagamiya, O. Hashimoto, *et al.*, Phys. Lett. B **53B**, 117 (1974).
15. T. N. Mamedov, V. N. Duginov, K. I. Gritsaj, *et al.*, JINR Commun. (Dubna), E14-2000-158 (2000).
16. T. N. Mamedov, D. Herlach, K. I. Gritsaj, *et al.*, Zh. Éksp. Teor. Fiz. **120**, 1086 (2001) [JETP **93**, 941 (2001)].
17. R. Abela, Hyperfine Interact. **87**, 1105 (1994).
18. Li Bai-Qin and Wang Ye-Ning, Phys. Rev. B **47**, 16582 (1993).
19. L. E. Drain, Philos. Mag. **4**, 484 (1959).
20. R. L. Odle and C. P. Flynn, Philos. Mag. **13**, 699 (1966).
21. S. Rubini, C. Dimitropoulos, and F. Borsa, Phys. Rev. B **49**, 12590 (1994).
22. S. Sotier, R. L. Odle, and J. A. Gardner, Phys. Rev. B **6**, 923 (1972).
23. R. A. Howe, D. A. Rigney, and C. P. Flynn, Phys. Rev. B **6**, 3358 (1972).
24. S. Rubini, C. Dimitropoulos, R. Gotthardt, and F. Borsa, Phys. Rev. B **44**, 2019 (1991).
25. S. Nagamiya, K. Nagamine, O. Hashimoto, and T. Yamazaki, Phys. Rev. Lett. **35**, 308 (1975).

Translated by R. Tyapaev

JETP Letters, Vol. 76, No. 12, 2002, pp. 697–699. Translated from Pis'ma v Zhurnal Éksperimental'noĭ i Teoreticheskoĭ Fiziki, Vol. 76, No. 12, 2002, pp. 825–827.

Left–Right Asymmetry of the Angular Distribution of Prompt Neutrons from ^{235}U Fission Induced by Polarized Thermal Neutrons

G. V. Danilyan, V. A. Krakhotin, V. S. Pavlov, and A. V. Fedorov

Institute of Theoretical and Experimental Physics, ul. Bol'shaya Cheremushkinskaya 25, Moscow, 117218 Russia

Received October 14, 2002; in final from, November 4, 2002

Left–right asymmetry of the angular distribution of prompt neutrons from ^{235}U fission induced by polarized thermal neutrons was measured. This asymmetry is caused by the interference of the *s* and *p* waves in the input reaction channel and was found to be equal to $b = (-5.8 \pm 1.4) \times 10^{-5}$. © *2002 MAIK "Nauka/Interperiodica".*

PACS numbers: 25.85.Ec

In our preceding paper [1], we reported the results of a search for *sp* interference in the emission of prompt neutrons from ^{235}U fission induced by polarized thermal neutrons. These results can be treated as evidence of the desired effect. The figure shows the geometry of the experiment.

The target is a $90 \times 220 \times 0.2$-mm aluminum plate both sides of which are covered with ^{235}U oxide–protoxide. The total content of ^{235}U in the target was 1.3 g. A collimated beam of thermal neutrons with a flux density of 10^5 cm^{-1} s^{-1} "slid" along the target. Fission fragments were detected by low-pressure multiwire proportional counters (the chamber was filled with hexane to a pressure of 3 torr). Delayed coincidences between pulses from a neutron detector (plastic scintillator and FEU-63) and detectors of fragments were measured. Time coincidences between fragments and prompt fission γ rays were discriminated from time of flight. Online measurements consisted of 15-min cycles; after each of them, the result of processing four time spectra (two for each neutron detector) was output to the display in the form of the asymmetry factor

$$b_i = (N_{1i} - N_{2i})/(N_{1i} + N_{2i}), \qquad (1)$$

where i is the detector number and N_1 and N_2 are the integrated neutron time spectra with two opposite polarizations.

Simultaneously, the averaged data with rms errors accumulated after the ith cycle were output to the display. Measurements over about 1000 h provided the desired asymmetry

$$b = (-5.8 \pm 1.4) \times 10^{-5}.$$

Theory [2] predicts various effects caused by the *s–p* interference in the input channel of the capture reaction of slow neutrons by nuclei. In particular, the angular distribution of particles c in the reaction $n + \mathrm{A} \longrightarrow \mathrm{C} + c$ of capturing polarized neutrons by nuclei A is given by the expression

$$W(\theta) = \mathrm{const}(1 + b\mathbf{s}[\mathbf{n}_{\mathrm{in}}, \mathbf{n}_c]), \qquad (2)$$

where $\mathbf{s}$ is the unit vector along the polarization of neutrons incident on the nucleus A and $\mathbf{n}_{\mathrm{in}}$ and $\mathbf{n}_c$ are the unit vectors along the momenta of the captured neutron and particle c, respectively.

Both the magnitude and sign of the coefficient b depend on the energy of neutrons captured by a nucleus, on the positions of the *s* and *p* resonances of the compound nucleus, and on the quantum characteristics of the initial and final states. For thermal neutrons and medium-heavy and heavy nuclei, the coefficient b is equal to about 10^{-4}. If several initial or final states contribute to the reaction, the coefficient b, when summed over these states, is less than for one state, because the coefficients can enter with opposite signs. We use this circumstance to search for so-called pre-fission or scission neutrons. The angular distribution of prompt fission neutrons is extended along the fission axis, i.e., along the momenta of fission fragments because of the composition of velocities. This property indicates that prompt neutrons are emitted primarily from excited completely accelerated fragments. However, some prompt neutrons have an almost spherically symmetric angular distribution, which indicates that they are emitted from the excited nucleus before its scission into two fragments. Experimental data on the fraction of these neutrons vary from 3 to 35% [3].

There are various assumptions about the emission mechanism of scission neutrons. Neutrons can be emitted upon "descending" from the saddle point to the nuclear configuration immediately before the rupture of the waist joining the two future fragments. In view of this circumstance, so-called triple fission, where light charged particles (p, d, t, ^{3}He, α, ^{5}He, etc.) are emitted together with two fragments, is noteworthy. The angu-

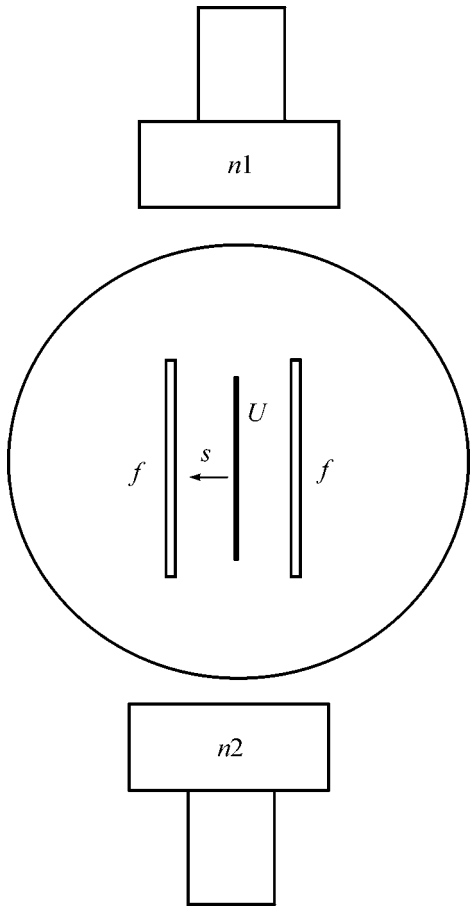

Geometry of the experiment: *U* is the ^{235}U target, *f* are the detectors of fission fragments, n_1 and n_2 are the detectors of prompt fission neutrons, and *s* is the polarization direction of a beam of thermal neutrons incident on the target perpendicular to the figure plane. Polarization direction was reversed every second.

lar and energy distributions of these particles follow from their focusing and acceleration in the Coulomb field of the two fragments. Therefore, they appear in the region between fragments. They are most likely emitted from the waist during its cooling. Obviously, neutrons can also be emitted through the same mechanism. Moreover, since the Coulomb barrier is absent for neutrons, the probability of neutron emission must be much higher than for protons. If such is the case, the fission process accompanied by the emission of neutrons from the waist can be treated as a neutral component of triple nuclear fission.

Recently, a collaboration including ITEP, Tübingen Universitat, Darmstadt Technische Universitat, PNPI, Kurchatov Institute, and Institut Laue–Langevin carried out a search experiment with the beam of polarized cold neutrons from the high-flux ILL reactor. In this experiment, the left–right asymmetry of α-particle emission about the plane determined by the polarization vector of fission-induced neutrons and the momentum of the light fragment was observed in the triple fission of the ^{233,235}U nuclei [4, 5]. The measured asymmetry was found to be about 10^{-3}. However, this value may increase to 10^{-2} if the degree of polarization of the fissioning nucleus is taken into account. The observed asymmetry can be described by the expression

$$W = \text{const}(1 + D\mathbf{s}[\mathbf{n}_{\text{lf}}, \mathbf{n}_\alpha]), \quad (3)$$

where $\mathbf{n}_{\text{lf}}$ and $\mathbf{n}$ are the unit vectors along the momenta of the light fragment and α particle, respectively.

Both Eqs. (1) and (2) are formally noninvariant upon time inversion. As for the *s–p* interference, theory implies that the coefficient *b* involves a phase factor that also changes its sign upon time inversion. If correlation (3) is caused by the interaction in the final state, the coefficient *D* must also involve phase. Unfortunately, triple fission is so complex that a rigorous theoretical explanation of the observed phenomenon is impossible. It only remains to experimentally examine this correlation in more detail.

In view of this circumstance, it is of interest to reveal the possible nature of the interaction in the final state of three charged particles. It can be either electromagnetic or strong. In the first case, a similar effect must obviously be absent in the neutral component of triple nuclear fission. Before preparing such an experiment, which requires an intense beam of polarized neutrons, it would be reasonable to verify that the neutral component of triple fission really exists. The observed *s–p* interference corroborates its existence, because final states are numerous and neutrons emitted by fragments cannot, therefore, exhibit *s–p* interference in the input reaction channel. The final states may be not so numerous both in the emission of α particles in triple fission and in the emission of pre-scission neutrons of double nuclear fission, so that the angular correlations may not tend to zero upon summing over these final states.

Being manifested in the left–right asymmetry of the angular distribution of fission fragments, the effect of *s–p* interference in the capture of polarized thermal neutrons by ^{235}U nuclei was measured in [6] and found to be on the order of 10^{-4}.[1] The same order of magnitude of the left–right asymmetry coefficient can be expected for a small number of final states in this process. The similar effect for fragment neutrons can be on the order of $10^{-4}/\sqrt{10^8} = 10^{-8}$. Nevertheless, the fragment neutrons are important in our measurements, because they cannot be discriminated from the scission neutrons. Inevitable background from the fragment neutrons decreases the measured asymmetry by a factor of $1 + \delta$, where δ is the fragment-to-scission neutron ratio. Therefore, the true asymmetry coefficient can be suppressed by a factor of 3 to 30, which is consistent

[1] The number of final states in the fission process is on the order of 10^8–10^{10}. However, the correlation is not suppressed, because it is formed at the stage of a cold strongly deformed pear-shaped nucleus at the saddle point, where the number of states for summation is small.

with the measured value $|b| = 5.8 \times 10^{-5}$. In addition, the result must be reduced to 100% nuclear polarization and corrected for the geometry of the experiment, which can provide one more order of magnitude. Of coarse, taking into account the difference between the spins of an α particle and neutron can also provide a more definite value of the asymmetry coefficient for neutrons. The coefficient δ can really be determined with a higher accuracy. Since the angular distributions of fragment and scission neutrons are substantially different, δ depends on the angle between the axis of fragment scattering and the direction to the neutron detector. The minimum background from fragment neutrons and, therefore, the maximum left–right asymmetry in the angular distribution of detected neutrons should be observed at 90°. Monte-Carlo simulation of an experiment with real geometry shows that measurement of the coefficients $b(90°)$ and $b(45°)$ with an accuracy of 10^{-6} will make it possible to determine both the true correlation coefficient and the fraction of scission neutrons among prompt fission neutrons with an accuracy of 10%. We are now preparing such an experiment.

We are grateful to Yu.A. Belov for technical help in the experiment and to the staff of the reactor at the Moscow Engineering Physics Institute, where the measurements with a polarized neutron beam were carried out. This work was supported by the Russian Foundation for Basic Research, project no. 00-02-16011.

REFERENCES

1. G. V. Danilyan, V. A. Krakhotin, V. S. Pavlov, and A. V. Fedorov, Pis'ma Zh. Éksp. Teor. Fiz. **74**, 448 (2001) [JETP Lett. **74**, 408 (2001)].
2. O. P. Sushkov and V. V. Flambaum, Usp. Fiz. Nauk **136**, 3 (1982) [Sov. Phys. Usp. **25**, 1 (1982)].
3. N. V. Kornilov, A. V. Kagalenko, and F.-J. Hambsch, in *Proceedings of VII International Seminar on Interaction of Neutrons with Nuclei, ISINN-7* (Dubna, 1999), p. 241 [or ISINN-9, 2001].
4. P. Jesinger, G. V. Danilyan, A. M. Gagarski, *et al.*, Yad. Fiz. **62**, 1723 (1999) [Phys. At. Nucl. **62**, 1608 (1999)].
5. G. V. Danilyan, A. V. Fedorov, A. M. Gagarski, *et al.*, Yad. Fiz. **63**, 1759 (2000) [Phys. At. Nucl. **63**, 1671 (2000)].
6. V. P. Alfimenkov, A. N. Chernikov, A. M. Gagarski, *et al.*, in *Proceedings of IV International Seminar on Interaction of Neutrons with Nuclei, ISINN-4* (Dubna, 1996), p. 120.

Translated by R. Tyapaev

JETP Letters, Vol. 76, No. 12, 2002, pp. 700–703. Translated from Pis'ma v Zhurnal Éksperimental'noĭ i Teoreticheskoĭ Fiziki, Vol. 76, No. 12, 2002, pp. 828–832.

Destruction of the Ozone Protecting Layer: Charge-Separation Mechanism in Clusters

S. V. Shevkunov

St. Petersburg State Technical University, ul. Politekhnicheskaya 29, St. Petersburg, 195251 Russia

e-mail: root@shevk.hop.stu.neva.ru

Received October 11, 2002; in final form, November 10, 2002

A model is constructed that explains the intense accumulation of chlorine in stratospheric ice microclusters. The model is approved in detail for quantitative consistency using Monte-Carlo computer simulation. A complex interparticle-interaction model is used that includes nonpair forces, charge transfer, and corrections for the quantum-statistical uncertainty in nuclear positions. In the presence of thermal fluctuations, two thermodynamically stable states of the HCl molecule—bound and dissociated—occur in water clusters. In clusters containing more than 35 water molecules, molecular dissociation into ions becomes thermodynamically favorable under the conditions of the polar stratosphere. © *2002 MAIK "Nauka/Interperiodica".*

PACS numbers: 92.60.Hp; 94.10.Fa; 82.33.Tb; 36.40.Ei; 64.60.Qb

The ozone layer protects Earth's surface from intense ultraviolet radiation. The ozone-depleted spots are more frequently formed in circumpolar regions, and their appearance correlates with seasonal temperature variations. According to modern observations [1, 2], the formation of "ozone holes" is preceded by the appearance of a specific accumulation of solid microparticles in the stratosphere at heights on the order of 100 km. The stratospheric cloud is composed, to a large extent, of ice microclusters. Analysis of natural observations in conjunction with laboratory studies [1–5] allows one to formulate the following most probable scenario of ozone destruction. Chlorine in chemical compounds inert with respect to ozone is accumulated in ice microcrystals. During seasonal warming, it is released and oxidized in the reaction with ozone. In photolytic reactions, the resulting chlorine compounds are again absorbed by ice microcrystals. Thus, the chlorine accumulated in the stratosphere is involved many times in repeated ozone-destruction cycles. The high adsorption ability of ice with respect to HCl, which is also measured in laboratory experiments [3–5], allows it to function for the destructive cycle as a whole. In recent years, the adsorption ability of ice has been the object of intensive study by both experimental methods [3–5] and computer simulation [6]. The data of measurements by different authors demonstrate a considerable scatter, which indicates a strong dependence of the properties of an ice adsorbing surface on the method of its preparation in laboratory conditions and on its microrelief. The phase state of ice surface layers at stratospheric temperatures is also not fully understood. The initial stage of capturing an HCl molecule from the gas phase is a bottleneck determining the rate of the entire process. Theoretically, two possible adsorption mechanisms exist for HCl: a simple physisorption and an adsorption with the preliminary ionic dissociation. In the second case, the strong electrostatic interaction between ions and the ice surface layers provides fast ion capture even at the initial stage. Computer simulation showed [6] that the simple physisorption is incapable of providing those high values of ice adsorption ability that are observed experimentally. The discrepancy achieves several orders of magnitude. The adsorption through the molecular ionic dissociation seems to be the most probable mechanism. Since the dissociation reaction requires overcoming an activation barrier, forces must exist which lead to the dissociation of the HCl molecule even in the gas phase.

Mere rupture of a chemical bond is insufficient for the charge separation. The dissociation requires overcoming Coulomb attraction between molecules, which may occur only upon its weakening in a solution. Water clusters formed from vapor in an electric field of a polar molecule provide the most favorable conditions for the gas-phase dissociation. After being dissolved in such a cluster, a molecule dissociates in it into ions, much as this occurs in a bulk electrolyte. Computer simulation shows [7–10] that the ionic electric field stabilizes water clusters.

In this work, the $H_3O^+(H_2O)_nCl^-$ cluster is modeled by the mechanostatistical Monte-Carlo method in a canonical statistical ensemble at temperatures 200 and 300 K. The interactions in the system are described using a specially developed complex pseudopotential model that implicitly incorporates the corrections for the quantum character of molecular motion and for the fluctuating-charge effect. The model takes into account nonpair interactions due to the partial collectivization of electronic shells, transfer of an excess charge, polar-

ization, hydrogen-bond formation, as well as the usual electrostatic interactions, exchange repulsion, and dispersion forces. A detailed description of the analytic form of potential interaction is beyond the scope of this publication; most of the terms are presented in detail in [7–10]. The numerical values of the ion–water interaction parameters were found by the method of successive approximations on the requirement that the agreement with the experimental data on free energy and enthalpy of water nucleation on the H_3O^+ and Cl^- ions [11, 12] be as accurate as possible. The cluster free energy was calculated by the method suggested in [13] for a bicanonical statistical ensemble and developed in the subsequent works. The numerical values for the parameters of direct interion interactions were taken so as to reproduce the cluster energies obtained by the quantum-chemical calculations for the complexes $HCl(H_2O)_n$ with $n = 1$, 2, and 3 [14]. A good agreement was obtained with both experimental data and quantum-chemical calculations. The free energy was reproduced with the experimental accuracy (fractions of k_BT).

To prevent cluster evaporation into vacuum, the system was placed in a spherical cavity with a radius of 20 Å, and the center of the hydroxonium ion was fixed inside the cavity to prevent direct contact of the cluster with the walls. The lengths of Markovian chains used for evaluating equilibrium mean values comprised 10–30 million molecular configurations, with the first 2–3 million being used for system thermalization. The cluster size was sequentially increased, and the last configuration of the preceding chain was used as the initial configuration of the running chain, with the subsequent thermalization.

The melting points of water clusters containing 20–40 molecules lie in the temperature range corresponding to the polar stratosphere. At the same time, the ionic electric field does not facilitate the cluster crystallization but, quite the reverse, can prevent transition to the ordered crystalline state [15]. The behavior of heat capacity, as calculated by the fluctuation theorem, and the calculation of the orientational correlation functions of molecules give evidence for a quasiliquid state of clusters under the conditions studied. The thermal fluctuations in such clusters play a crucial role, so that the use of a mechanostatistical description is necessary.

The mean force potential $W(R, T)$ between ions separated by the distance R has the meaning of interaction energy, which includes not only the direct but also all the interactions produced via the cluster molecules and averaged over molecular positions and ion orientations. The mean force potential is related to the ion–ion correlation function $g_{+-}(R; T)$ by the familiar formula

$$W(R, T) = k_BT\ln(g_{+-}(R; T)) + \text{const}. \qquad (1)$$

The Monte-Carlo calculation of $W(R, T)$ was performed by the direct averaging of the total energy of the system for a pair of ions fixed at various distances R. The

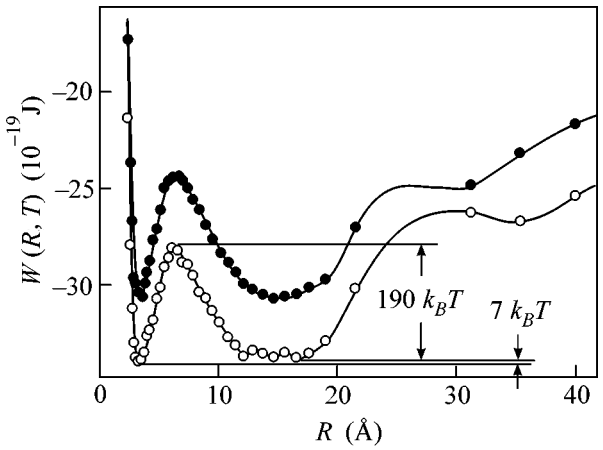

Fig. 1. Mean force potential of the hydroxonium and chlorine ions in the $H_3O^+(H_2O)_{30}Cl^-$ cluster vs. distance between the ions; (○) 200 and (●) 300 K.

$W(R, T)$ curve shows two deep minima with a strong maximum between them (Fig. 1). The positions of these minima correspond to the stable ion positions inside the cluster. The closest minimum at $R = 3.6$ Å corresponds to two ions with a distance between them close to their contact. This distance is 0.47 Å larger than the equilibrium distance between the ions in vacuum; the water molecules slightly force the ions apart. The second minimum is situated at a distance close to 15 Å. This minimum corresponds to the stable ion positions in the dissociated state of HCl. The presence of this minimum is indicative of a possible dissociation of a molecule. The position of the first minimum is almost independent of the cluster size, whereas the second minimum shifts to larger distances approximately proportionally to the cluster linear size. Those ion positions for which most of the molecules are situated in the interion region, while the ions are near the surface, are thermodynamically favorable. As the cluster size decreases, the second minimum becomes shallower and fully disappears in the clusters with $n < 5$. The calculated ion–ion correlation functions show sharp maxima in the regions of minima, with half-widths of ~0.5 Å at the first minimum and ~1 Å at the second. These values give an estimate for the characteristic value of the fluctuations of interion distance. Upon rising to room temperature, the character of R dependence does not change for $W(R, T)$, although the curve, as a whole, rises approximately by 3×10^{-19} J.

The change in the average separation between the ions upon varying the cluster size is presented in Fig. 2 for the dissociated states of the HCl molecule. These states were selected through the preliminary thermalization of the system in a configuration with ions separated by a distance of 20 Å. This was followed by thermalization in the regime of nonfixed ions, after which mean values were calculated. A barrier separating the dissociated states from bound states in clusters with

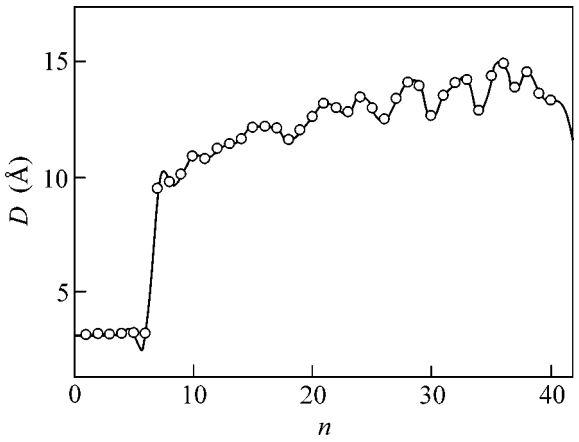

Fig. 2. Average distance between the hydroxonium and chlorine ions in the $H_3O^+(H_2O)_nCl^-$ clusters vs. cluster size for the dissociated states at a temperature of 200 K.

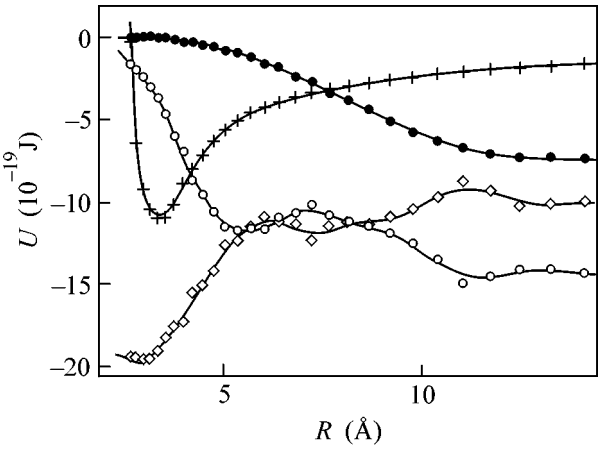

Fig. 3. Different types of interaction constituting the mean force potential for the hydroxonium and chlorine ions in the $H_3O^+(H_2O)_{30}Cl^-$ cluster at a temperature of 200 K; (○) H_3O^+–water molecules, (●) Cl^-–water molecules, (+) H_3O^+–Cl^-, and (◇) interaction energy between the water molecules and water molecules with ions.

$n > 6$ prevented the ion recombination during the simulation session. In the clusters with $n \le 6$, the ions draw close together to a contact distance under the action of electric attractive forces and expel water molecules from the interion region. One can see from Fig. 2 that, after changing the cluster size by one molecule (from $n = 6$ to $n = 7$), the separation between ions increases fourfold jumpwise, and the ions are stabilized at distances corresponding to the second minimum of $W(R, T)$. On further increase in the cluster size, the ions continue to draw apart. In the clusters with $n > 20$, the average interion distance slightly oscillates with changing cluster size, evidencing the microstructuring. At room temperature, the same dependence with a jump is also observed at the same point $n = 7$, but the variations in interion distances become smoothed.

The stabilization mechanism of the dissociated HCl state in water clusters can be understood from a comparison of the behavior of different energy components of the system when the ions are pushed apart. The first minimum of $W(R, T)$ is mainly due to the direct ion–ion and water–water interactions (Fig. 3). The main contribution to the second minimum of $W(R, T)$ comes from the ion–water interactions (Fig. 3), with the interaction between the hydroxonium ion and water molecules in the dissociated state being twice as strong as for the chlorine ion. In the bound state, these energies differ from each other by a factor of 20. The hydroxonium ion plays a leading part in the stabilization of both the dissociated state and the cluster as a whole. In the bound state of the HCl molecule, the ion's hydrate shell is almost destroyed by the hydroxonium ion field, and the dipole moments of molecules are pointed away from the ion pair. Water molecules form a hydrogen-bond network, with the pronounced preferred orientation of dipole moments along the ion field lines. To stabilize the dissociated state of HCl, no less than three molecular layers should be situated between ions. The structures stable at zero temperature with a monomolecular layer between the H_3O^+ and Cl^- ions [14] are incapable of stabilizing the system at stratospheric temperatures. The two minima corresponding to the bound and dissociated molecular states are separated by a high maximum with a height of $190k_BT$. The kinetic characteristics, including the characteristic time of overcoming this barrier as a result of thermal fluctuations, cannot be calculated by the Monte-Carlo method. Nevertheless, one can expect that this time is on the same order as the dissociation time of a molecule in a bulk water solution; i.e., the thermodynamic equilibrium between these two states is established on a macroscopic time scale. The relative statistical weights of states depend exponentially on the difference between their free energies. For estimation, it suffices to compare their internal energies. The internal energy of the dissociated state in a cluster with $n = 30$ molecules is $7k_BT$ times higher, but this difference decreases with increasing n. The point where this difference changes sign, i.e., the cluster size for which the dissociated state becomes energetically more favorable than the bound state, can be determined by extrapolating to the intersection of the graphs of internal energies of the bound and dissociated states. One can see from Fig. 4 that, as the cluster size increases, the energies of both states, being negative, decrease, although the energy of the dissociated state decreases faster. The intersection point corresponds to $n = 37$; however, considering that the entropy of the dissociated state is higher, one should expect that the latter will become thermodynamically more favorable for the clusters containing $n = 35$–36 water molecules. Therefore, HCl dissociates to form chlorine ions in clusters with $n > 35$ molecules. Our preliminary calculations

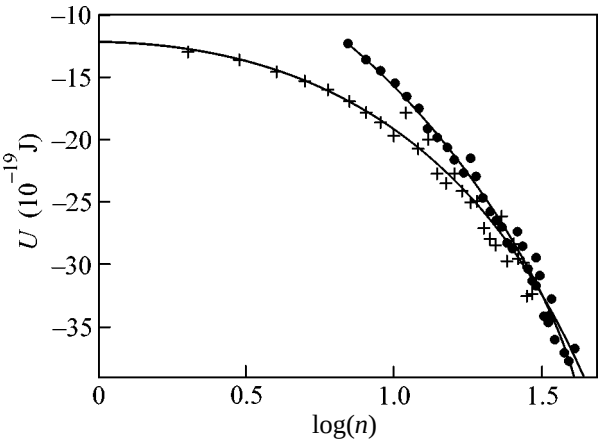

Fig. 4. Total interaction energy in the $H_3O^+(H_2O)_nCl^-$ clusters at a temperature of 200 K vs. the cluster size for two states of HCl molecule; (●) dissociated and (+) bound state.

suggest that the clusters of this size in a field of two counterions are situated at the boundary of the stable equilibrium with saturated vapor. This fact explains the deciding role of such clusters in the accumulation kinetics of chlorine ions: all chlorine ions pass through the ion-pair hydration stage. One should expect that a relatively sharp decrease in temperature will lead to the formation of a saturated layer near the surface of ice microparticle and to an increase of the stable cluster size in the ion field, which, in turn, will shift the dynamic equilibrium toward the HCl dissociation and fast chlorine-ion adsorption on the ice surface. It is conceivable that this mechanism is precisely that which provides the relatively high sensitivity of the chlorine adsorption and emission at the surface of ice microparticles to the seasonal temperature variations in the stratosphere.

The stability of the hydrate shell of a chlorine ion in water vapor near the adsorbing surface was studied separately. The free energy and the hydration work were calculated. In the saturated vapor, drawing together of the ion and surface is accompanied by linking the hydrate shell to the surface and its fast growth across the surface. Simultaneously, the molecules of the hydrate shell form a sort of "cocoon" covering the ion. Thus, the chlorine ion proves to be built-in under the surface layer even at the initial stage of the process.

This work was supported by INTAS, grant no. 99-01162.

REFERENCES

1. S. M. Solomon, R. R. Garcia, F. S. Rowland, and D. J. Wuebbles, Nature **321**, 755 (1986).
2. D. C. Clary, Science **271**, 509 (1996).
3. H. A. Dansig, D. Herridge, and J. C. Vickerman, J. Phys. Chem. A **102**, 2302 (1998).
4. M.-T. Leu, L. F. Keyser, and R. S. Timonen, J. Phys. Chem. B **101**, 6259 (1997).
5. B. Fluckinger, L. Chaix, and M. J. Rossi, J. Phys. Chem. A **104**, 11739 (2000).
6. G. J. Kroes and D. C. Clary, J. Phys. Chem. **96**, 7079 (1992).
7. S. V. Shevkunov, Dokl. Akad. Nauk **379**, 181 (2001) [Dokl. Phys. **46**, 467 (2001)].
8. S. V. Shevkunov, Zh. Éksp. Teor. Fiz. **119**, 485 (2001) [JETP **92**, 420 (2001)].
9. S. V. Shevkunov, Kolloidn. Zh. **62**, 569 (2000).
10. S. V. Shevkunov and A. Vegiri, Mol. Phys. **98**, 149 (2000).
11. Y. K. Lau, S. Ikuta, and P. Kebarle, J. Am. Chem. Soc. **104**, 1462 (1982).
12. M. Arshadi, R. Yamdagni, and R. Kebarle, J. Phys. Chem. **74**, 1475 (1970).
13. S. V. Shevkunov, A. A. Martsinovskiĭ, and P. N. Vorontsov-Vel'yaminov, Teplofiz. Vys. Temp. **26**, 246 (1988).
14. S. Re, Y. Osamura, and Y. Suzuki, J. Chem. Phys. **109**, 973 (1998).
15. S. V. Shevkunov, Kolloidn. Zh. **63**, 560 (2001).

Translated by V. Sakun

JETP Letters, Vol. 76, No. 12, 2002, pp. 704–706. From Pis'ma v Zhurnal Éksperimental'noĭ i Teoreticheskoĭ Fiziki, Vol. 76, No. 12, 2002, pp. 833–835.

Standing Waves and Reflectivity from an Ultrathin Layer¶

M. A. Andreeva[1, *] and B. Lindgren[2]

[1]*Faculty of Physics, Moscow State University, Moscow, 117234 Russia*

**e-mail: marina@ttk.ru*

[2]*Department of Physics, Uppsala University, Uppsala, 75121 Sweden*

Received November 6, 2002

We have analytically found that the reflectivity amplitude from one thin layer in the presence of the other reflecting layers is modulated by the squared amplitude of the radiation field but not by the first-order amplitude, as was supposed in the paper of R. Röhlsberger (Hyperfine Interactions **123**/**124**, 455 (1999)), for delayed nuclear resonance reflectivity. Hence, a larger sensitivity to standing waves is expected for the reflectivity signal from selected groups of atoms or nuclei compared with the secondary radiation emission. © *2002 MAIK "Nauka/Interperiodica".*

PACS numbers: 61.10.Kw; 68.49.Uv

Standing waves are created when an incident wave is coherently reflected from crystals or multilayers (diffraction, total external reflection for X rays and neutrons). This effect has long been effectively used for investigation of the depth position of a selected group of atoms by means of secondary radiation (fluorescent signal, photoelectrons) [1, 2].

Recently, it has become possible to select the contribution from selected group of atoms *in the reflectivity signal itself* by investigation of the spectrum of reflectivity or by selection of the scattering channel (e.g., nuclear resonant scattering is selected from the electronic scattering by time gating [3]). Since the first experiment, where a peak near the critical angle of the total external reflection in delayed nuclear resonant reflectivity was observed, the idea of the influence of standing waves on the reflectivity signal itself has been discussed [4–7]. Investigations of the shape of the time spectra of Bragg reflectivity and its variation with angle [8, 9] also led the authors to the conclusion that the energy or time dependence of standing waves inside a periodical resonant multilayer influences the reflectivity energy or time spectrum [10]. Several experiments with resonant ^{57}Fe layers embedded at different depths in thin magnetic films have been performed in which the enhancement of the reflectivity signal due to the creation of standing waves near the critical angle was used [11, 12]. The influence of standing waves on the reflectivity signal is even more substantial in the new type of measurements recently performed by Röhlsberger *et at.* [13], where ^{57}Fe layers are placed inside a wave-guide structure. In all such measurements, the reflectivity signal was investigated and not the secondary radiation. All authors in [4–13] imply that a connection between standing waves and delayed nuclear resonant reflectivity exists, but no analytical expressions were derived, with the exception of [7], where such an expression was suggested, but the wrong one (as we show here).

Here we have got an analytical expression which describes the "standing-wave influence" on the reflectivity signal from an ultrathin layer in the presence of the other reflecting layers. It is essential that the reflectivity cannot be considered as secondary radiation emission, because in reflectivity measurements the detected radiation is coherent with the incident radiation, and it obeys the laws of propagation in a layered medium.

The most understandable result can be obtained from the kinematic approximation for reflectivity [14], where we simply add the reflectivity amplitudes from individual layers with an appropriate phase factor:

$$R = \sum_n r_n e^{2i\varphi_n}. \quad (1)$$

The reflectivity from a thin layer r_n is described by the well-known expression [15]

$$r = i\frac{\lambda}{\sin\vartheta}\rho f, \quad (2)$$

where λ is the wavelength of radiation, ϑ is the glancing angle, ρ is the surface density of scattering centers, and f is the forward scattering amplitude by a single scattering center.

At a first sight, the contribution from each layer to the reflectivity in (1) is independent from the others. But let us consider the contribution to the total reflectivity R^{tot} from one additional layer on top of a multi-

¶This article was submitted by the authors in English.

layer or other substrate with the reflectivity R. The result will be the following:

$$R^{\text{tot}} = R\exp\left(iQd + i\frac{2\lambda\rho}{\sin\vartheta}f\right) + r \cong R' + r(1 + 2R'), \tag{3}$$

where $Q = (4\pi/\lambda)\sin\vartheta$, d is the thickness of the layer. In (3), we also took into account the phase and refraction corrections of the total reflectivity caused by the added layer through the phase factor $2i\varphi$ (the approximation used is valid for the angular region beyond the critical angle ϑ_c of the total external reflection):

$$2\varphi = \frac{4\pi}{\lambda}\eta d,$$
$$\eta = \sqrt{\sin^2\vartheta + \frac{\lambda^2}{\pi}\rho_v f} \cong \sin\vartheta + \frac{\lambda^2}{2\pi\sin\vartheta}\rho_v f, \tag{4}$$

and we used the determination $\rho = \rho_v d$ (ρ_v is the volume density of the scattering centers). R' in (3) is the reflectivity R at the distance d from the top of the multilayer (relative to the incident wave at the same height):

$$R' = Re^{iQd}. \tag{5}$$

For very thin layers, we can neglect this phase factor. However, (5) can be generalized for the case when the added layer is placed at some distance H from the surface. In this case, d in (5) is replaced by H. It is this phase factor that determines the angular or depth variations of the standing waves. The above consideration can easily be repeated for the thin layer placed inside the multilayer.

For illustration we consider a resonant ^{57}Fe layer on top of nonresonant superstructure [Si/W] · 20. The calculated spectrum of Mössbauer reflectivity $R^{\text{tot}}(\omega)$ is determined by $r(\omega)$ and by the position H of the resonant layer relative to the surface of the superstructure (through the phase shift between the amplitudes of scattering R' and $r(\omega)$). The standing-wave influence appears through the complex factor $(1 + 2R')$ modulating $r(\omega)$ (Fig. 1). This factor enhances the contrast of the spectrum when a ^{57}Fe layer is placed at the antinode of a standing wave (Fig. 1a) and suppresses it at the node (Fig. 1b).

So in the kinematic approximation (when the reflectivity R is small enough), the change of the single-layer scattering amplitude caused by the other layers in the multilayer is described by the factor $(1 + 2R')$. This result already shows up the difference of the reflectivity and the secondary radiation emission, because the amplitude of the last one is proportional to the amplitude of the radiation field $(1 + R')$.

For angles close to the critical angle, the kinematic approximation in the reflectivity theory is not valid. We should use here the exact Parratt recursive formula for reflectivity amplitude:

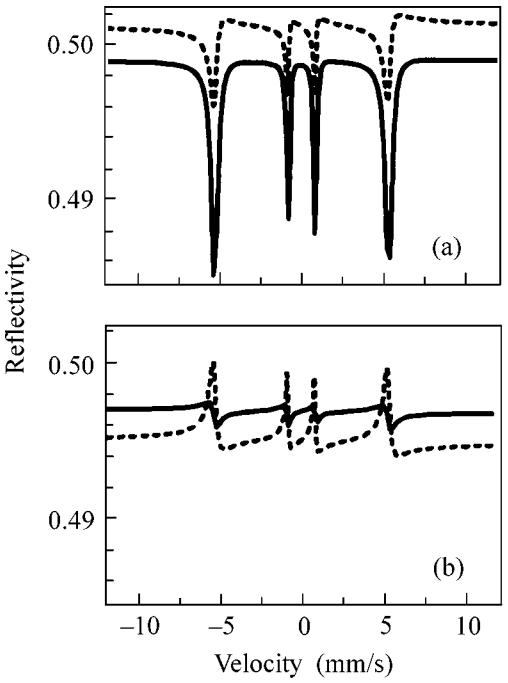

Fig. 1. Calculated Mössbauer spectra of reflectivity at the exact Bragg angle 14.75 mrad from a thin ^{57}Fe layer placed at the distance (a) $H = D/2$ and (b) $H = 0$ from the surface of a multilayer with period $D = 3.0$ nm (solid lines). Dashed lines correspond to the pure interference of $r(\omega)$ and R without the standing-wave factor $(1 + R)^2$.

$$R_j = \frac{r_j + R_{j+1}e^{2i\varphi_j}}{1 + r_j R_{j+1}e^{2i\varphi_j}}. \tag{6}$$

Here, r_j is the Fresnel reflectivity amplitude, R_{j+1} is the multiple reflectivity amplitude at the previous boundary, the expression for the phase shift φ_j is given by (4), but the approximate formula for the square root cannot be used now.

For calculation of the reflectivity from a thin layer by (6), we suppose that $2i\varphi$ is small. In order to simplify the calculations, we insert an artificial vacuum buffer layer with zero thickness between the tested layer and substrate, although the algebra can also be carried out without this layer. Neglecting the $(2i\varphi)^2$ term, we obtain

$$R^{\text{tot}} = \frac{r_{01} + \tilde{R}}{1 + r_{01}\tilde{R}} + \frac{\tilde{R}(1 - r_{01}^2)}{(1 + r_{01}\tilde{R})^2}2i\varphi_1 \tag{7}$$

and

$$\tilde{R} = \frac{r_{10} + R}{1 + r_{10}R}, \tag{8}$$

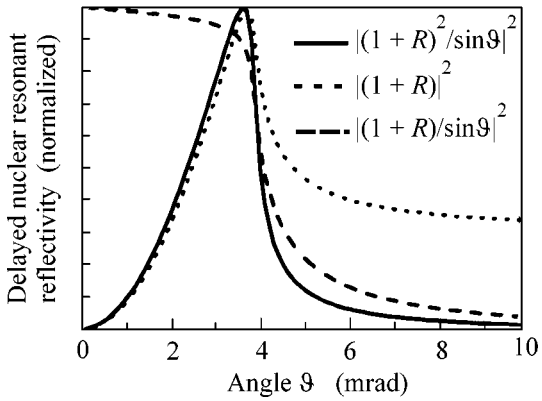

Fig. 2. The integral nuclear resonant reflectivity from a thin ^{57}Fe layer on top of a nonresonant ^{56}Fe substrate (solid line) calculated by means of Parratt formula (6), which gives exactly the same result as (9). Notice that the factor $1/\sin\vartheta$ appears from (2). The dotted line is the dependence suggested by Röhlsberger [7] if we neglect the $1/\sin\vartheta$ factor in r (the well-known dependence for secondary radiation emission [2]); the dashed line is the dependence if we do not neglect this factor (no peak at the critical angle ~3.7 mrad appears).

where r_{01} is the Fresnel reflectivity amplitude from the tested layer and R is the reflectivity amplitude from the substrate. Finally, we obtain

$$R^{\text{tot}} = R(1 + iQd) + (1 + R)^2 r, \qquad (9)$$

where r is again determined by (2).

The obtained result is surprisingly simple and clear. The layer reflectivity amplitude r in the presence of the other reflecting layers is modulated by the "squared standing wave" $(1 + R)^2$, because the standing-wave structure of the radiation field reveals itself for the incident (absorption process) as well as for reflected wave (emission process). The kinematic approach obtained above (3) is true when R is small and $(1 + R)^2 \approx 1 + 2R$.

The obtained formula (9) differs from the analogous expression (4.1) presented in [7]:

$$R^{\text{tot}} = R + (1 + R)(r - r_S) \qquad (10)$$

(we have rewritten it here in our notation and note that r_S is determined by Eq. (2) but with the substrate parameters). Expression (10) from [7] implies that the reflected amplitude from a thin layer is proportional to the amplitude of the total radiation field $(1 + R)$ (the unessential term r_S can be effectively combined with R), just as in the case of secondary radiation emission. The correct expression (9) contains this amplitude squared $(1 + R)^2$.

If we again suppose that the investigated thin layer is the resonant layer ($r = r(\omega)$), then the delayed nuclear resonance reflectivity is calculated by the Fourier transform of (9), which gives

$$\left|R^{\text{tot}}(t)\right|^2 = \left|(1 + R)^2\right|^2 |r(t)|^2. \qquad (11)$$

In Fig. 2, we plot the result of the calculations by formula (9) and (10) (formula (4.2) from [7]). We see that (10) does not give the right behavior of the delayed nuclear resonance reflectivity in any case.

Of course, calculations can be performed correctly by the main formula (6), but the importance of the presented expression (9) is that it clarifies the physical understanding of how the reflectivity from a thin layer is changed in the presence of the other reflecting substance. It also directly shows the role of standing waves in the reflectivity process. The illustrations here were given for the case of nuclear resonant reflectivity experiments, but the result also refers to any kind of reflectivity measurements, e.g., magnetic X-ray scattering, neutron reflectivity, and so on.

The authors are grateful to A.I. Chumakov for stimulating discussions and R. Röhlesberger for presenting [13] before publication. This work was supported by the Royal Swedish Academy of Sciences, the Russian Foundation for Basic Research (grant no. 01-02-17541), and INTAS (grant no. 01-0822).

REFERENCES

1. M. V. Koval'chuk and V. G. Kohn, Usp. Fiz. Nauk **149**, 69 (1986) [Sov. Phys. Usp. **29**, 426 (1986)].
2. M. J. Bedzyk, G. M. Bommarito, and J. S. Schildkraut, Phys. Rev. Lett. **62**, 1376 (1989).
3. See the review issue of Hyperfine Interact. **123–124** (1999); in particular the basic introduction is given by G. V. Smirnov, Hyperfine Interact. **123–124**, 31 (1999).
4. A. Q. R. Baron, J. Arthur, S. L. Ruby, *et al.*, Phys. Rev. B **50**, 10354 (1994).
5. T. S. Toellner, W. Sturhahn, R. Röhlsberger, *et al.*, Phys. Rev. Lett. **74**, 3475 (1995).
6. M. A. Andreeva, Phys. Lett. A **210**, 359 (1996).
7. R. Röhlsberger, Hyperfine Interact. **123–124**, 455 (1999).
8. M. A. Andreeva, S. M. Irkaev, V. G. Semenov, *et al.*, J. Alloys Compd. **286**, 322 (1999).
9. M. A. Andreeva, S. M. Irkaev, V. G. Semenov, *et al.*, Hyperfine Interact. **126**, 343 (2000).
10. M. A. Andreeva, Pis'ma Zh. Éksp. Teor. Fiz. **69**, 816 (1999) [JETP Lett. **69**, 863 (1999)]; Surf. Investig. **16**, 9 (2001).
11. L. Niesen, A. Mugarza, M. F. Rosu, *et al.*, Phys. Rev. B **58**, 8590 (1998).
12. R. Röhlsberger, J. Bansmann, V. Senz, *et al.*, Phys. Rev. Lett. **86**, 5597 (2001).
13. R. Röhlsberger, H. Thomas, K. Schlage, *et al.*, Phys. Rev. Lett. **89**, 237201 (2002).
14. I. W. Hamley and J. S. Pedersen, J. Appl. Crystallogr. **27**, 29 (1994).
15. V. I. Iveronova and G. P. Revkevich, *The Theory of X-Ray Scattering* (Mosk. Gos. Univ., Moscow, 1972), Chap. 3.

JETP Letters, Vol. 76, No. 12, 2002, pp. 707–710. Translated from Pis'ma v Zhurnal Éksperimental'noĭ i Teoreticheskoĭ Fiziki, Vol. 76, No. 12, 2002, pp. 836–839.

Resonance Modes of Layered Ferromagnets in a Transverse Magnetic Field

V. F. Meshcheryakov

Moscow State Institute of Radio Engineering, Electronics, and Automation (Technical University), Moscow, 117454 Russia

e-mail: niin@ranet.ru

Received November 6, 2002

Intensities and positions of resonance lines are calculated for the ferromagnetic resonance spectra of multilayer ferromagnetic films in a magnetic field oriented normally to the film surface. It is shown that the positions of spectral lines depend on the number of ferromagnetic layers, while the line intensities are determined by the phase shift between the oscillations of the magnetic moments of neighboring layers. A qualitative comparison is carried out between the results of calculations and the spectra observed in experiments. © *2002 MAIK "Nauka/Interperiodica".*

PACS numbers: 76.50.+g; 75.70.–i

Ferromagnetic resonance (FMR) serves as one of the methods of studying multilayer ferromagnetic films characterized by a giant magnetoresistance. For FMR, ferromagnetic layers separated by a nonmagnetic metal interlayer represent an analogue of the coupled resonance circuits. Therefore, as in multiply connected circuits, the number of resonance modes observed in FMR must correspond to the number of ferromagnetic layers.

In multilayer films, experimental observations reveal only one line, which is interpreted as a line corresponding to the homogeneous resonance. Additional resonance modes were observed in such systems only in a limited number of cases, when the static magnetic field was oriented along the film plane (parallel configuration). To excite additional modes, a high-frequency field was applied along the static field. In films consisting of two ferromagnetic layers, optical modes were studied in [1], and in Fe/Cr multilayer systems, additional modes were observed in [2]. Our attempt to observe these modes for similar Fe/Cr samples in a magnetic field oriented normally to the film plane (perpendicular configuration) failed, because the FMR lines broadened and vanished as this direction was approached.

In Co/Cu polycrystalline multilayers exposed to static (perpendicular to the film plane) and high-frequency (parallel to the film surface) magnetic fields, we repeatedly observed several resonance lines [3]. At the same time, additional resonance lines were absent in the parallel configuration. Figure 1 shows the shapes of the FMR spectra obtained for two samples in the perpendicular configuration at a frequency of 9.55 GHz. The samples were obtained by magnetron sputtering on a single-crystal silicon substrate and consisted of 15 Co/Cu layer pairs. The samples differed in the thickness of the nonmagnetic interlayer: [Co(30 Å)/Cu(9 Å)] × 15 (sample 1) and [Co(30 Å)/Cu(12 Å)] × 15 (sample 2). For sample 1, in addition to the main line, several weak lines were observed at lower fields. Their intensities monotonically decreased with decreasing resonance field. In the case of sample 2, the line intensities differed little from each other, and the line widths were almost ten times smaller than those observed for sample 1. The measurements of the magnetization of these films, along with the angular dependence of the spectrum, showed that only the main line observed in sample 1 corresponds to the homogeneous resonance. The structural studies of the film cross sections, which were performed by transmission electron microscopy [3], revealed a clearly pronounced layered structure in sample 1. In sample 2, the layered structure was much less pronounced, and, on the background of this weakly pronounced layered structure, no regular alternation of layers was observed.

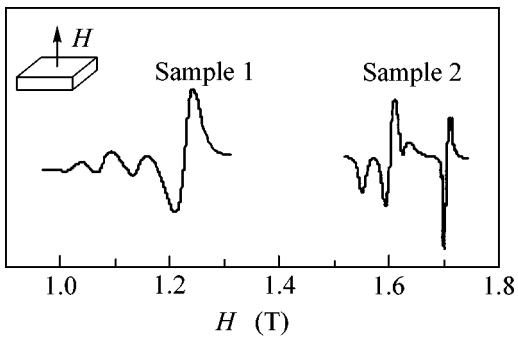

Fig. 1. Derivatives of the absorption spectra for two samples which differ in the thickness of the Cu interlayer; the magnetic field is oriented normally to the film plane.

Calculated positions of spectral lines for films containing different numbers of layers

Number of layers	Resonance conditions
1	$\omega_1/\gamma = H_0$
2	$\omega_1/\gamma = H_0$, $\omega_{2,3}/\gamma = \pm(H_0 - 2H_E)$
3	$\omega_1/\gamma = H_0$, $\omega_{2,3}/\gamma = \pm(H_0 - 2H_E)$, $\omega_{4,5}/\gamma = \pm(H_0 - 3H_E)$
4	$\omega_1/\gamma = H_0$, $\omega_{2,3}/\gamma = \pm(H_0 - 2H_E)$, $\omega_{4,5,6,7}/\gamma = \pm(H_0 - 3H_E \pm \sqrt{2}H_E)$
5	$\omega_1/\gamma = H_0$, $\omega_{2,3,4,5}/\gamma = \pm(H_0 - \frac{3 \pm \sqrt{5}}{2}H_E)$, $\omega_{6,7,8,9}/\gamma = \pm(H_0 - \frac{5 \pm \sqrt{5}}{2}H_E)$
6	$\omega_1/\gamma = H_0$, $\omega_{2,3}/\gamma = \pm(H_0 - H_E)$, $\omega_{4,5}/\gamma = \pm(H_0 - 2H_E)$, $\omega_{6,7}/\gamma = \pm(H_0 - 3H_E)$, $\omega_{4,5,6,7}/\gamma = \pm(H_0 - 2H_E \pm \sqrt{3}H_E)$

The description of additional modes is based on the spin-wave concept. According to [4], spin waves occur in multilayer films only when the magnetic field is oriented normally to the film surface. As in single-layer films, their spectrum is described by the equation [4]

$$\frac{\omega}{\gamma} = H - K_{\text{eff}}M_S - \frac{A}{M_S} \cdot \mathbf{k}^2, \qquad (1)$$

where A is the modified constant of exchange interaction in the ferromagnetic layer, $K_{\text{eff}} = (4\pi + 2U/M_S^2)$ is the coefficient characterizing the energy of demagnetizing field and the uniaxial anisotropy U, and $\mathbf{k}$ is the wave vector whose magnitude is proportional to an integer. These modes were observed experimentally [5] in Co/Cu multilayer samples near the perpendicular orientation of magnetic field. The measured spectrum was adequately described by Eq. (1), and the intensity of spectral lines with $k \neq 0$ was much lower than the intensity of the homogeneous resonance line. In our experiment mentioned above, additional modes were observed in sample 1 also near the perpendicular configuration, but the wave vector was not proportional to an integer. According to the model proposed by Wigen *et al.* [6], the magnetic moments in each ferromagnetic layer are directed parallel to each other and oscillate with a certain phase shifted relative to the oscillations of moments in other layers. In the same publication, it was shown that, in the perpendicular configuration, the width of the calculated spectrum depends on the total number of layers and is doubled when the number of layers changes from two to infinity. The relative intensities of the resonance lines were not calculated.

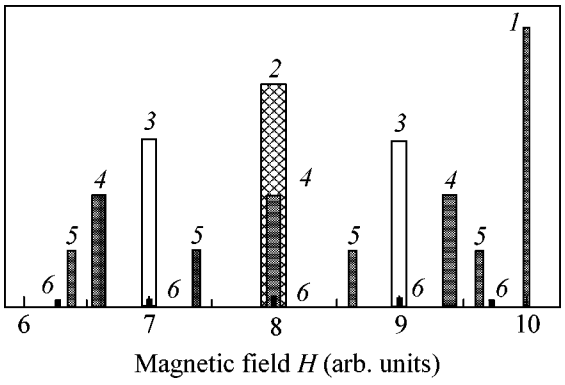

Fig. 2. Relative positions of the resonance modes in the perpendicular configuration for films with equal values of $H_E > 0$. Columns of equal height correspond to films with equal numbers of ferromagnetic layers. The numbers near the columns indicate the number of layers in the film. Column *1* corresponds to the resonance line of a single-layer film and to the homogeneous resonance line ($\omega_1/\gamma = H_0$) for a multilayer film.

Using the aforementioned model, in which a kth ferromagnetic layer possesses its own magnetization $\mathbf{M}_k$, it is possible to calculate the resonance spectrum of a multilayer system with alternating layers in the perpendicular configuration. We represent the energy of the system in the form

$$E = -\mathbf{H}\sum_k \mathbf{M}_k + \frac{J_1}{dM_S^2}\sum_{k \neq j}\mathbf{M}_k\mathbf{M}_j + \frac{J_2}{dM_S^4}\sum_{k \neq j}(\mathbf{M}_k\mathbf{M}_j)^2 + \frac{K_{\text{eff}}}{2}\sum_k M_{kz}^2, \qquad (2)$$

where the z axis is directed normally to the film surface, H is the magnetic-field strength, J_1 and J_2 are the exchange-interaction constants, and d is the ferromagnetic-layer thickness. Assuming that the magnetic field and the magnetizations of all layers are directed along the z axis, i.e., normally to the film plane, and using the equation of motion for magnetization, we obtain the resonance spectrum. The spectra calculated in this way for films with different numbers of layers are presented in the table, where the following notation is introduced: $H_0 = H - K_{\text{eff}}M_S$ and $H_E = J_1/dM_S + 2J_2/dM_S$. According to the formulas shown in the table, Fig. 2 displays (in columns) the relative positions of the resonance modes obtained for films with equal values of $H_E > 0$. Column *1*

corresponds to the positions of the resonance line of a single-layer film and of the homogeneous resonance line $\omega_1/\gamma = H_0$ of a multilayer film. The numbers given near the columns in Fig. 2 indicate the corresponding numbers of layers in the films. As one can see from this figure, an increase in the number of layers is accompanied by an increase in the spectrum width, unlike the case of the spin-wave spectrum. Positions of lines with different numbers of layers are different, which disagrees with the calculations performed in [5].

To describe the shape and intensity of the lines in resonance spectrum, it is necessary to calculate the imaginary part of the total high-frequency susceptibility for various values of the phase φ_j of magnetic moment oscillations. Let us direct the high-frequency component of magnetic field along the *x* axis. Then, we represent the high-frequency magnetization components of the *j*th layer in the form $\mathbf{m}_j = \mathbf{m}_{oj} \cdot \exp(i(\omega t + \varphi_j))$ and introduce into the equation of motion the terms describing the damping of the transverse magnetization components in the form of the Bloch–Bloembergen equations (m_{jx}/T, m_{jy}/T). In the case of homogeneous oscillations ($\varphi = \varphi_j - \varphi_{j+1} = 0$), the spectrum consists of a single line, irrespective of the number of layers. For films consisting of two and three ferromagnetic layers, the spectra were calculated for different phase shifts φ between neighboring layers. In the case of a two-layer film, an increase in the phase shift is accompanied by a decrease in the intensity of the homogeneous resonance line and an increase in the intensity of the line corresponding to the so-called optical mode. At $\varphi = 180°$, only one optical mode is observed. For a three-layer film, we assume that the phase shifts between different pairs of neighboring layers are equal. Figure 3 presents the results of calculating the spectrum of a three-layer film for different phase shifts. As the phase shift increases, the intensity of the homogeneous resonance line decreases and additional modes arise; first one closely lying mode appears and then another. An increase in the phase shift leads to a decrease in the intensity of the homogeneous resonance line, so that the latter disappears at $\varphi = 120°$. Note that, at a certain phase shift ($\varphi = 180°$), the central spectral line is also absent. In the spin-wave theory, the additional lines observed in the spectrum are interpreted as modes each corresponding to a particular wave number. In our case, all spectral lines are excited for a given phase difference, and their intensities are determined by the difference in the phases of magnetic moment oscillations in neighboring layers.

As an example, Fig. 4 shows the FMR spectrum observed at a frequency of 9.55 GHz in the perpendicular configuration for a Cu(200 Å)/Co(25 Å)/Cu(38 Å)/Co(25 Å) polycrystalline film deposited on a single-crystal silicon substrate. Line *2* shows the derivative of the absorption spectrum calculated using the following parameters: $g = 2.13$, $K_{\text{eff}}M_S = 13440$ Oe, $H_E = -250$ Oe, $T = 1.34 \times 10^{-10}$ s, $\varphi = 127°$, and $f = 9.55 \times 10^9$ Hz.

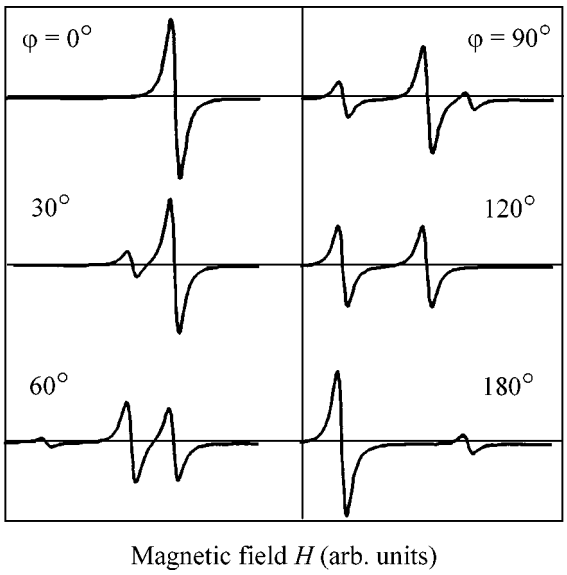

Fig. 3. Derivatives of the FMR absorption spectra of a film consisting of three ferromagnetic layers calculated for different values of phase shift. The magnetic field is oriented normally to the film surface. The values used in the calculations for the phase shift between the magnetization oscillations in neighboring layers are indicated in the plot. The line intensities are presented in absolute units.

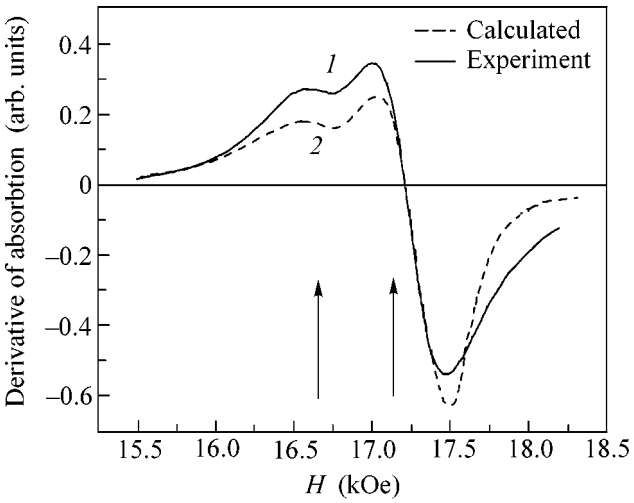

Fig. 4. Derivatives of the FMR absorption spectra of a film consisting of two ferromagnetic layers in a magnetic field oriented normally to the film surface: (*1*) experiment and (*2*) calculation with the parameters $g = 2.13$, $K_{\text{eff}}M_S = 13440$ Oe, $H_E = -250$ Oe, $T = 1.34 \times 10^{-10}$ s, $f = 9.55 \times 10^9$ Hz, and $\varphi = 127°$. The arrows indicate the positions of the spectral lines.

The mechanism responsible for the phase difference between the magnetization oscillations may be the non-

collinear ordering of the high-frequency magnetization components in neighboring layers, because the component of static field in this direction is zero. As in the case of the magnetostatic modes, the orientation of a high-frequency magnetization in a magnetic field perpendicular to the sample plane is determined by the magnetostatic interactions in the film plane. In addition, according to [7], each layer can be divided into domains, which may also cause a noncollinear ordering of the high-frequency magnetizations of neighboring layers. Therefore, the noncollinearity may result from both the presence of the third term in Eq. (2) and the presence of domains. The latter are determined, to a great extent, by the local inhomogeneities arising in the course of film fabrication.

The results obtained from the calculations qualitatively agree with the spectra observed in the experiment (Fig. 1). In sample 1, where the most regular and clearly defined layered structure is observed, the intensity of the additional modes is noticeably lower than the intensity of the homogeneous resonance line, and the positions of these modes are ordered. This indicates that the phase shift between the oscillations in neighboring regions does not exceed several tens of degrees (see Fig. 3 for $\varphi = 30°$). Hence, the misorientation of the neighboring regions in zero magnetic field must be of the same order of magnitude. In sample 2, in which an irregular layered structure is observed, the phase shift between the oscillations in neighboring regions is much greater than in sample 1 and comprises more than a hundred degrees (see Fig. 3 for $\varphi = 120°$). The spectral lines are positioned chaotically, and, according to the previously obtained results, the homogeneous resonance line is absent.

In other experiments [2, 8], we studied additional modes of oscillation in Fe/Cr multilayer films in the parallel configuration. In magnetic fields below the critical field H_c, where the magnetizations of the neighboring layers were directed at an angle to each other, the oscillation spectrum exhibited additional lines. In the fields $H > H_c$, these lines were absent. On the basis of the results obtained above, this disappearance of additional lines can be understood as the result of the alignment of magnetizations of all layers with the external magnetic field.

Thus, the calculations performed for the FMR spectra of multilayer films suggest that

(1) In layered structures, the spectrum of magnetic moment oscillations is determined by the number of weakly coupled ferromagnetic regions and the strength of exchange interaction between them;

(2) The intensity of the spectral lines depends on the phase shift between the oscillations of magnetic moments in neighboring regions. The phase shift is determined by the magnetostatic interactions and the domain structure in the film plane. The domain structure is determined, to a great extent, by the local inhomogeneities in the film composition, which arise in the course of film fabrication;

(3) In the general case, the resonance lines observed experimentally cannot be interpreted as lines corresponding to a specific value of phase shift. Exceptions are the homogeneous resonance line and the optical mode for a two-layer film.

I am grateful to A.I. Morozov and Yu.K. Fetisov for discussing the results. The work was supported by the Russian Foundation for Basic Research, project no. 00-02-17162.

REFERENCES

1. S. M. Rezende, C. Chesman, M. A. Lucena, *et al.*, J. Magn. Magn. Mater. **177–181**, 1213 (1998).
2. A. B. Drovosekov, N. M. Kreĭnes, V. F. Meshcheryakov, *et al.*, Pis'ma Zh. Éksp. Teor. Fiz. **67**, 690 (1998) [JETP Lett. **67**, 727 (1998)].
3. V. F. Meshcheryakov, A. G. Vasil'ev, K. V. Timonin, and I. A. Khorin, Kristallografiya **47**, 1119 (2002) [Crystallogr. Rep. **47**, 1063 (2002)].
4. R. P. van Stapele, F. J. A. M. Greidanus, and J. W. Smits, J. Appl. Phys. **57**, 1282 (1985).
5. Z. J. Wang, S. Mitsudo, K. Watanabe, *et al.*, J. Magn. Magn. Mater. **176**, 127 (1998).
6. P. E. Wigen and Z. Zhang, Braz. J. Phys. **22**, 267 (1992).
7. V. D. Levchenko, A. I. Morozov, and A. S. Sigov, Zh. Éksp. Teor. Fiz. **121**, 1149 (2002) [JETP **94**, 985 (2002)].
8. A. B. Drovosekov, O. V. Zhotikova, N. M. Kreĭnes, *et al.*, Zh. Éksp. Teor. Fiz. **116**, 1817 (1999) [JETP **89**, 986 (1999)].

Translated by E. Golyamina

JETP Letters, Vol. 76, No. 12, 2002, pp. 711–715. Translated from Pis'ma v Zhurnal Éksperimental'noĭ i Teoreticheskoĭ Fiziki, Vol. 76, No. 12, 2002, pp. 840–845.

Effective Mass of Quasiparticles in a Wigner Liquid

É. G. Batyev

Institute of Semiconductor Physics, Siberian Division, Russian Academy of Sciences, pr. Akademika Lavrent'eva 13, Novosibirsk, 630090 Russia

e-mail: batyev@isp.nsc.ru

Received October 21, 2002; in final form, November 19, 2002

The exchange interaction and effective mass of fermionic excitation in a low-density ($r_S \gg 1$) system of two-dimensional electrons are estimated from simple considerations. For the ratio of effective (renormalized due to interaction) to band mass, the dependence $m^*/m = (A/\sqrt{r_S})\exp(\alpha\sqrt{r_S})$ is obtained, where A and α are constants on the order of unity. The effective g factor is independent of r_S and is larger than its bare value in the two-valley case (silicon). Comparison with experimental data shows a qualitative agreement with silicon. © *2002 MAIK "Nauka/Interperiodica".*

PACS numbers: 71.27.+a; 71.10.Pm

In recent years, the properties of low-density two-dimensional electrons (holes) have been intensively studied (see, e.g., review [1]). Since this system is characterized by strong interaction, the effective mass and g factor may differ appreciably from their bare values and, moreover, strongly change with density. This was confirmed experimentally in [2–6], where the corresponding dependences on carrier concentration were obtained. This work is devoted to the theoretical consideration of these questions.

In a low-density electron system, the Coulomb interaction is strong compared to the kinetic energy (at zero temperature). The ratio of these energies is on the order of the average distance between particles in Bohr radii r_S (provided that the kinetic energy is estimated as in a Fermi gas). Low densities correspond to $r_S \gg 1$. At sufficiently large values of r_S, a Wigner crystal is formed. It is shown in [7] that this occurs at $r_S > 37 \pm 5$. At smaller, though large values of r_S, a strongly correlated liquid appears (sometimes called a Wigner liquid) with short-range order, as in crystal. It is this state which will be the subject of this work.

It is conventional to describe such a liquid in terms of the Landau theory of Fermi liquid. This implies that the elementary excitations are classified as in a Fermi gas; i.e., due to the interaction of Fermi-type excitations, their properties (e.g., effective mass or spin susceptibility) are different from the properties of fermionic excitations in gas. Although the Landau theory of Fermi liquid provides the appropriate general relations, the question arises as to whether one can draw more detailed conclusions about the Wigner liquid. In this work, an attempt is made to answer this question.

In a strongly correlated system of interest, a particle resides for a time in the minimum of a potential produced by the surroundings, after which it jumps occasionally into the other minimum. This is reminiscent of the behavior of a particle in the strong-coupling model, which is used to calculate electronic spectrum in a crystal, where the effective mass m^* is given by

$$m^* \sim 1/|t|a^2, \tag{1}$$

where t is the hopping matrix element and a is the lattice constant. In our problem, this hopping occurs through the positional exchange of two neighboring particles, and, thus, there is a need to determine the level exchange splitting energy, which will play the role of matrix element t. The assumed analogy with the behavior of a particle in a periodic field is the key idea of this work.

To illustrate this idea, the following should be noted. The above-mentioned exchange interaction should play a decisive role in the particle transport in a strongly correlated quantum liquid, like a Wigner liquid. Then a relation of type (1) (where a is the average distance between particles) follows from mere dimensional considerations. It is implied that a quasiparticle moves as a free particle (with weak damping as in the theory of a Fermi liquid) and does not diffuse, as, e.g., in the classical system (note parenthetically that these two limiting possibilities also occur for a particle in crystal).

One more remark should be made in this respect. Imagine that the system is completely spin-polarized (by a longitudinal magnetic field) and we are interested in the motion of a particle with inverted spin. To this end, one should know the exchange interaction with the nearest neighbors. In a crystal, this quantity would suffice to determine the spin-wave spectrum. In a liquid (homogeneous system), a quasiparticle can be assigned momentum, so that charge moves together with spin. It hence follows that, knowing the exchange interaction,

one may hope to make a correct estimate of the quasiparticle effective mass.

If the exchange energy is known for two particles, one can use Eq. (1) to estimate the effective mass and, as it appears, draw certain conclusions about the exchange interaction of quasiparticles in a Fermi liquid, namely, about its sign and concentration dependence. It is the main purpose of this work to obtain corresponding relations. Agreement of the theoretical conclusions with the available experimental data is also discussed.

So, one should first of all estimate the exchange interaction. Since, in the low-concentration limit considered, it is weaker than the Coulomb interaction and smaller than the characteristic plasma frequency, the problem of its determination can be highly simplified. The following model is then suggested. Let us choose two neighboring particles and replace their interaction with others by some effective external field, which we will take in the simplest possible way, while their mutual interaction will be of the Coulomb type, as it is in reality. With this approach, the problem becomes single-particle, and it can be solved in the quasiclassical approximation.

In the simplified formulation, the Hamiltonian of a system of two particles is chosen in the form

$$H = \frac{-1}{2m}(\nabla_1^2 + \nabla_2^2) + \sum_{i=1}^{2} \frac{m(\omega_1^2 x_i^2 + \omega_2^2 y_i^2)}{2} + \frac{e^2}{\epsilon|\mathbf{r}_1 - \mathbf{r}_2|}. \quad (2)$$

Here, m is the band mass, the second term is the external field simulating the influence of other particles (plus the compensating charge), and the frequencies $\omega_{1,2}$ are chosen so that the equilibrium distance between the particles (in the classical limit) corresponds to the average distance between the particles of the system. Let these minima be situated on the x axis at the points $\pm a/2$ (a is the equilibrium distance between the particles in the classical limit). Apart from this condition, the parameters of the model are also determined from the requirement that the potential minimum of one of the particles be isotropic for a fixed position of another particle. This gives

$$\omega_1^2 = \frac{2e^2}{\epsilon m a^3}, \quad \omega_2^2 = \frac{5\omega_1^2}{2}. \quad (3)$$

Let us introduce the center-of-gravity coordinates and the relative coordinates:

$$x_{1,2} = X \pm x/2, \quad y_{1,2} = Y \pm y/2. \quad (4)$$

One can see that the wave function of the system with Hamiltonian (2) is the product of functions of the (X, Y) and (x, y) coordinates, with the function of the first pair of coordinates being known, while the wave function of the second pair is determined from the Schrödinger equation with the Hamiltonian

$$H_0 = \frac{-1}{2\mu}\nabla^2 + \frac{\mu(\omega_1^2 x^2 + \omega_2^2 y^2)}{2} + \frac{e^2}{\epsilon r}, \quad (5)$$

where $\mu = m/2$ is the reduced mass. Hence, the problem is simplified; one should now consider the motion of a single particle in the oscillatory field and in the field of repulsive Coulomb center that is situated at the origin of coordinates. The potential minima are at the points $\pm a$ on the x axis.

In the leading approximation, the ground-state wave function for a particle positioned near the right minimum has the form

$$\psi_+(x, y) \sim \exp\left[-\frac{\mu\Omega_1}{2}(x-a)^2 - \frac{\mu\Omega_2}{2}y^2\right], \quad \Omega_1^2 = 3\omega_1^2, \quad \Omega_2^2 = \frac{3}{2}\omega_1^2. \quad (6)$$

Next we will follow the standard methods (see, e.g., the problem of hydrogen molecular ion in book [8], Ch. XI). Let Ψ_S and Ψ_A be, respectively, symmetric and antisymmetric functions of coordinates and correspond to the eigenenergies E_S and E_A, so that the equations for them have the form

$$E_S\Psi_S = H_0\Psi_S, \quad E_A\Psi_A = H_0\Psi_A. \quad (7)$$

The function Ψ_A changes sign, while Ψ_S does not change upon the substitution $x \longrightarrow -x$. Multiplying the first equation by Ψ_A and the second equation by Ψ_S, subtracting one from the other term-by-term, and then integrating over the half plane $x > 0$, one gets

$$E_S - E_A = \frac{1}{\mu}\int dy\left(\Psi_A\frac{\partial\Psi_S}{\partial x} - \Psi_S\frac{\partial\Psi_A}{\partial x}\right)_{x=0}.$$

This result can be rewritten after introducing the functions

$$\Psi_{1,2} = \frac{1}{\sqrt{2}}(\Psi_S \pm \Psi_A) \quad (8)$$

(we will assume that the function Ψ_1 is mainly concentrated near the right minimum). Then we have for the energy difference

$$E_S - E_A = \frac{1}{\mu}\int dy\left(\Psi_1\frac{\partial\Psi_2}{\partial x} - \Psi_2\frac{\partial\Psi_1}{\partial x}\right)_{(x=0)}. \quad (9)$$

The functions $\Psi_{1,2}$ transform into one another upon the substitution $x \longrightarrow -x$. For this reason, Eq. (9) can be rewritten as

$$E_S - E_A = \frac{-2}{\mu}\int dy\left(\Psi_1\frac{\partial\Psi_1}{\partial x}\right)_{(x=0)}. \quad (10)$$

Therefore, one must determine the function Ψ_1 near $x = 0$ on the condition that this function coincides with Ψ_+ (6) near the right minimum.

Let us now turn to the solution of the equation with Hamiltonian (5). We first discuss the properties of potential energy using the cylindrical coordinates (r, φ). For a fixed φ, the potential grows as $r \longrightarrow 0, \infty$, and the minimum is achieved at $r = r_m$, for which

$$r_m^3 = \frac{e^2}{\epsilon\mu(\omega_1^2\cos^2\varphi + \omega_2^2\sin^2\varphi)}. \quad (11)$$

We now go to dimensionless coordinates ($r/a = \rho$) and measure energy in units $e^2/\epsilon a$. In these units, one has, instead of Eq. (5),

$$\frac{\epsilon a}{e^2}H_0 \longrightarrow h_0 = \frac{-1}{2M}\left\{\frac{1}{\rho}\frac{\partial}{\partial\rho}\left(\rho\frac{\partial}{\partial\rho}\right) + \frac{1}{\rho^2}\frac{\partial^2}{\partial\varphi^2}\right\} + \frac{(1 + (3/2)\sin^2\varphi)\rho^2}{2} + \frac{1}{\rho}, \quad M = \frac{\mu e^2 a}{\epsilon} \quad (12)$$

($M \sim r_S \gg 1$). The presence of a large value M will be used below in the approximate solution to the problem.

The wave function $\Psi(\rho, \varphi)$ is sought in the form

$$\Psi(\rho, \varphi) = \psi(\rho, \varphi)/\sqrt{\rho}.$$

The function ψ obeys the equation

$$\frac{-1}{2M}\left\{\frac{\partial^2}{\partial\rho^2} + \frac{1}{\rho^2}\frac{\partial^2}{\partial\varphi^2} + \frac{1}{4\rho^2}\right\}\psi + \left\{\frac{(1 + (3/2)\sin^2\varphi)\rho^2}{2} + \frac{1}{\rho}\right\}\psi = E\psi. \quad (13)$$

For the moment, this is an exact equation of the model. Its solution will be analyzed by simplifying Eq. (13) as far as possible using the fact that $M \gg 1$. The desired dependence will be obtained in the leading approximation (except for a constant coefficient). The simplification amounts to the neglect of small contributions. Namely, the contribution $1/4\rho^2$ is omitted in the first term, because it is small compared to the second term on the left-hand side of the equation; the potential energy is expanded in powers of ρ in the vicinity of the minimum; finally, in the coefficient of the second derivative with respect to φ, ρ is replaced by its value in the potential minimum. It is convenient to pass to the new variable $\xi = \rho - \rho_m$. This gives

$$\frac{-1}{2M}\left\{\frac{\partial^2}{\partial\xi^2} + \frac{1}{\rho_m^2}\left(\frac{\partial}{\partial\varphi} - \rho_m'\frac{\partial}{\partial\xi}\right)^2\right\}\psi + \left\{\frac{3}{2\rho_m} + \frac{F(\varphi)\xi^2}{2}\right\}\psi = E\psi, \quad (14)$$

$$\rho_m^3 = 1/(1 + (3/2)\sin^2\varphi), \quad \rho_m' = \frac{d\rho_m}{d\varphi}.$$

Here, $\rho_m = r_m/a$ (see Eq. (11)). The quantity $F(\varphi) \sim 1$, and its exact value will not be required in the approximations adopted.

Let us separate out in Eq. (14) the part that depends on ξ and contains derivatives only with respect to ξ. Introduce the functions $\chi_n(\xi, \varphi)$, where φ is a parameter and which are solutions to the equation

$$\frac{-1}{2M}\left\{\left(1 + \frac{\rho_m'^2}{\rho_m^2}\right)\frac{\partial^2}{\partial\xi^2} - \frac{\rho_m''}{\rho_m^2}\frac{\partial}{\partial\xi}\right\}\chi_n + \frac{F(\varphi)\xi^2}{2}\chi_n = \epsilon_n(\varphi)\chi_n.$$

By the transformation $\chi \longrightarrow \exp(a\xi)\chi$, where the quantity $a(\varphi)$ is chosen so that the first derivative vanishes ($a \sim 1$), this equation reduces to the familiar equation for an oscillator. As a result, one has for the spectrum

$$\epsilon_n(\varphi) = (n + 1/2)\Omega(\varphi) + b(\varphi),$$

where $\Omega(\varphi) \sim 1/\sqrt{M}$ and $b(\varphi) \sim 1/M$.

The functions χ_n are orthogonal with weight $\exp(-2a\xi)$. The solution to Eq. (14) can be sought in the form

$$\psi(\xi, \varphi) = \sum_n \Phi_n(\varphi)\chi_n(\xi, \varphi).$$

Since the limiting form of the function $\psi(\xi, \varphi)$ in the vicinity of the potential minimum is known (Eq. (6)), only the ground state is retained in the sum

$$\psi(\xi, \varphi) = \Phi_0(\varphi)\chi_0(\xi, \varphi). \quad (15)$$

The equation for Φ_0 is obtained in the standard manner: Eq. (15) is substituted into Eq. (14) and Eq. (14) is multiplied by χ_0, whereupon the integration is performed with respect to ξ. Considering that χ_0 is the oscillator ground-state function (with displaced center), one has for this function

$$\int d\xi\left(\chi_0\frac{\partial\chi_0}{\partial\xi}\right) = 0,$$

so that the contribution containing the first derivative $\partial\Phi_0/\partial\varphi$ vanishes. The contribution to the potential

energy in the φ direction from the integral

$$\int d\xi\left(\chi_0\frac{\partial^2\chi_0}{\partial\varphi\partial\xi}\right)\sim 1$$

(with the normalized function χ_0) multiplied by $\sim 1/M \ll 1$ can be neglected. As a result, one has the following equation for Φ_0:

$$\frac{-1}{2M\rho_m^2}\frac{\partial^2\Phi_0}{\partial\varphi^2}+\left\{\frac{3}{2\rho_m}+\epsilon_0(\varphi)\right\}\Phi_0 = E\Phi_0. \qquad (16)$$

The function Φ_0 in the classically inaccessible region can be calculated in the quasiclassical approximation [8]. Inasmuch as we are interested in the functional behavior and not in the constant coefficients, the small quantity $\epsilon_0(\varphi) \sim 1/\sqrt{M}$ can be ignored at a large distance from the turning point and E can be replaced, with the same accuracy, by the value of potential energy at the minimum; i.e., $E \longrightarrow 3/2$. As a result, one obtains for Φ_0 in the vicinity of the point of interest $\varphi = \pi/2$ (see Eq. (10))

$$\Phi_0(\varphi)\sim\exp\left(-\int_0^\varphi d\varphi\sqrt{3M(\rho_m-\rho_m^2)}\right). \qquad (17)$$

Next we use Eq. (10) (going from ψ to Ψ_1) or an analogous formula to obtain (directly using Φ_0) the dimensionless energy difference. Note that there are two contributions from two trajectories (the function Ψ_1 has two maxima at the positive and negative values of y). As a result, one obtains for the energy difference (except for a factor on the order of unity)

$$E_S-E_A\sim-\frac{\sqrt{M}}{\mu a^2}\exp\left(-2\int_0^{\pi/2}d\varphi\sqrt{2M(\rho_m-\rho_m^2)}\right). \qquad (18)$$

Correspondingly, the effective mass is estimated, according to Eq. (1), as

$$\frac{m^*}{m}\sim\frac{1}{\sqrt{M}}\exp\left(2\int_0^{\pi/2}d\varphi\sqrt{3M(\rho_m-\rho_m^2)}\right), \qquad (19)$$

or, after evaluating the integral in the exponent,

$$\frac{m^*}{m}\sim\frac{1}{\sqrt{M}}\exp(1.76\sqrt{M}).$$

This is the result of a simplified approach with Hamiltonian (2). In the general case, one can only state that

$$\frac{m^*}{m} = \frac{A}{\sqrt{r_S}}\exp(\alpha\sqrt{r_S}), \qquad (20)$$

where the coefficients A and α are on the order of unity. The expression obtained is valid at $r_S \gg 1$. Note that a similar dependence can be derived from general considerations, if one takes into account that tunneling proceeds in the vicinity of a certain trajectory, whose parameters are known within an order of magnitude, after which a comparison should be made with the one-dimensional case. The approximations adopted in the approach used in this work are quite clear and, in principle, the result can be refined.

From comparison of Eqs. (18) and (19), one gets

$$|E_S-E_A|\sim\frac{n}{m^*}\sim\epsilon_F,$$

where n is the carrier concentration and ϵ_F is the Fermi energy. Since the characteristic velocity of quasiparticles in liquid is the Fermi velocity v_F, the characteristic travel time τ at the distance a between the particles can be estimated as

$$\tau\sim a/v_F\sim 1/\epsilon_F\sim 1/|E_S-E_A|.$$

Thus, the time τ is found to be on the order of the particle residence time, as it must. This indicates that the use of Eq. (1) for estimating the quasiparticle effective mass in liquid is not contradictory but, rather, gives a reasonable result.

It follows from the Landau theory of Fermi liquid that spin polarization of the Fermi liquid in a magnetic field is determined by the effective g factor g^* (more precisely by the product g^*m^*). Once the estimate of the exchange interaction of two particles is obtained, an attempt can naturally be made to understand what will happen with quasiparticles in a Fermi liquid, i.e., what one can say about g^*. We are interested mainly in a two-valley system. In this case, a particle is characterized, apart from its spin **S**, by the valley number. This situation can be described by introducing the quasispin half-**Q** operator. In the case of two particles, the exchange interaction H_{ex} can be generally written as

$$H_{ex} = \lambda_S(\mathbf{S}_1\mathbf{S}_2)+\lambda_Q(\mathbf{Q}_1\mathbf{Q}_2) + \lambda_{SQ}(\mathbf{S}_1\mathbf{S}_2)(\mathbf{Q}_1\mathbf{Q}_2) \qquad (21)$$

(indices 1 and 2 label particles). In this expression, the invariance under the independent rotations in the spin and quasispin spaces is taken into account (complete spin and valley degeneracy is assumed). The total wave function must be antisymmetric about the particle permutations. As usual, this poses limitations on the possible spin and quasispin states.

Let us introduce the total spin and quasispin, $\mathbf{S} = \mathbf{S}_1 + \mathbf{S}_2$ and $\mathbf{Q} = \mathbf{Q}_1 + \mathbf{Q}_2$. For the spatially symmetric state with energy E_S, states with quantum numbers ($S = 1$, $Q = 0$) and ($S = 0$, $Q = 1$) are possible, while for the spatially antisymmetric state with energy E_A, states with quantum numbers ($S = 1$, $Q = 1$) and ($S = 0$, $Q = 0$) are possible. One can readily verify that the relations between the coefficients of Eq. (21) and the exchange level splitting are as follows:

$$\lambda_S = \lambda_Q = \lambda_{SQ}/4 = (E_A-E_S)/2. \qquad (22)$$

Now, the following conclusions can be drawn on the properties of Fermi liquids. For crystals (in the ground state), it would be reasonable to consider the lowest-energy states of nearest neighbors ($S = 1$, $Q = 0$) and ($S = 0$, $Q = 1$). Then the states with the maximal spin and the maximal quasispin would be degenerate. This degeneracy could be removed, e.g., by a weak magnetic field, which would result in a complete spin polarization. In a Fermi liquid with short-range order as in crystals, this tendency will be retained with the appropriate corrections caused by the contribution from the kinetic energy of quasiparticles. Therefore, one can conclude that, in a Fermi liquid with two valleys, the quasiparticle interaction will be of the ferromagnetic type; i.e., the effective g factor will be greater than in gas ($g^* > g$).

Moreover, in the limit $r_S \gg 1$, the effective g factor is independent of r_S ($g^* = \text{const}$). This follows from the Landau theory of Fermi liquid and our statement that the dependence of exchange interaction, which is determined by the difference $|E_S - E_A|$, coincides with the dependence of $1/m^*$. However, one cannot determine a numerical change in the g factor, because the results obtained in this work have a qualitative character, so that one can speak only about the type of dependences and the orders of magnitude.

A comparison with the result obtained, e.g., in [2] (Eq. (1) of this work) allows one to determine the coefficients in the r_S dependence of g^*m^* (and, correspondingly, of the spin susceptibility χ^*):

$$\frac{\chi^*}{\chi} = \frac{g^*m^*}{gm} \approx \frac{0.59}{\sqrt{r_S}}\exp(0.95\sqrt{r_S}) \qquad (23)$$

(the r_S values considered in [2] were, probably, not too large). This formula yields values that are lower than given in [3, 4], where the results were obtained for a broader range of r_S values. As for g^*, the results $g^* \approx$ const and $g^* > g$ obtained in [4] are in agreement with our conclusions, whereas in [3] g^* increases with r_S.

For the one-valley case, only the behavior of the effective g factor changes: it should be smaller than its bare value. However, this is at variance with the experiments performed in [5, 6]. The most surprising thing is that the effective mass obtained in [5, 6] virtually does not change with an increase in r_S ($m^* \approx m$). It is likely that this disagreement is caused by the fact that the spin–orbit interaction in GaAs is considerable (this is also noted in [5] in connection with other questions), and this fact was not taken into account in our considerations.

Of interest is to compare with the numerical Monte-Carlo results. In [9], a broad range of r_S values was considered. Contrary to [7] (and to our conclusions), the transition (at $r_S \approx 26$) to the spin-polarized state was obtained in the liquid phase. Let us compare the results obtained for the spin susceptibility for the r_S values different from the indicated value, by using Eq. (5) in [9], the expression following from Eq. (20) of this work, and the conclusion that g^* is constant. The agreement becomes quite good in the range $5 < r_S < 18$, if the coefficients are taken, e.g., in the following way:

$$\frac{\chi^*}{\chi} \approx \frac{0.26}{\sqrt{r_S}}\exp(1.43\sqrt{r_S}).$$

This is an analogue of Eq. (5) in [9], which involved six parameters. Note that the value $\alpha \approx 1.43$ in this expression is rather close to that obtained in the model with $\alpha \approx 1.72$ (see Eq. (19) and below), if the distance between the nearest neighbors in a triangle lattice is substituted for the interparticle separation a. In Eq. (23), the dissimilarity from the model value is greater, but the comparison with the results obtained in [3, 4], likely, could give the better agreement (such a comparison has not been carried out as yet). As for the pre-exponential factor, in the one-valley case (as in [9]), this factor should be smaller than in the two-valley case, as follows from our conclusion about the behavior of g^* in these cases (it either increases or decreases). It seems that this tendency takes place if one compares the last expression with Eq. (23).

I am grateful to M.V. Éntin for helpful discussions. This work was supported by the Russian Foundation for Basic Research (project no. 02-02-16159), INTAS (grant no. 2212), and the program "Physics of Solid-State Nanostructures."

REFERENCES

1. E. Abrahams, S. V. Kravchenko, and M. P. Sarachik, Rev. Mod. Phys. **73**, 251 (2001).
2. T. Okamoto, K. Hosoya, S. Kawaji, and A. Yagi, Phys. Rev. Lett. **82**, 3875 (1999).
3. V. M. Pudalov, M. E. Gershenson, H. Kojima, *et al.*, Phys. Rev. Lett. **88**, 196404 (2002).
4. A. A. Shashkin, S. V. Kravchenko, V. T. Dolgopolov, and T. M. Klapwijk, Phys. Rev. B **66**, 073303 (2002).
5. E. Tutuc, S. Melinte, and M. Shayegan, Phys. Rev. Lett. **88**, 036805 (2002).
6. Y. Y. Proskuryakov, A. K. Savchenko, S. S. Safonov, *et al.*, Phys. Rev. Lett. **89**, 076406 (2002).
7. B. Tanatar and D. M. Ceperley, Phys. Rev. B **39**, 5005 (1989).
8. L. D. Landau and E. M. Lifshitz, *Course of Theoretical Physics*, Vol. 3: *Quantum Mechanics: Non-Relativistic Theory*, 4th ed. (Nauka, Moscow, 1989; Pergamon, New York, 1977).
9. C. Attaccalite, S. Moroni, P. Gori-Giorgi, and G. B. Bachelet, Phys. Rev. Lett. **88**, 256601 (2002).

Translated by V. Sakun

JETP Letters, Vol. 76, No. 12, 2002, pp. 716–719. From Pis'ma v Zhurnal Éksperimental'noĭ i Teoreticheskoĭ Fiziki, Vol. 76, No. 12, 2002, pp. 846–849.

A New Class of Nodal Stationary States in a 2D Heisenberg Ferromagnet¶

I. G. Bostrem and A. S. Ovchinnikov*

Department of Theoretical Physics, Ural State University, Ekaterinburg, 620083 Russia

** e-mail: alexander.ovchinnikov@usu.ru*

Received September 30, 2002; in final form, November 27, 2002

A new class of nodal topological excitations in a 2D Heisenberg model is studied. The solutions correspond to a nodal singular point of the gradient field of the azimuthal angle. An analytical solution is found for the isotropic case. The effect of in-plane exchange anisotropy is studied numerically. This results in solutions which are analogues of the conventional out-of-plane solitons in 2D magnets. © *2002 MAIK "Nauka/Interperiodica".*

PACS numbers: 75.10.Hk; 75.30.Kz

The known topological solutions in the two-dimensional (2D) Heisenberg model belong to classes of the homotopic groups isomorphic to the group of integers such as $\pi_2(S^2)$: Belavin–Polyakov (BP) solitons [1] and easy-axis solitons [2]; to the relative homotopic group $\pi_2(S^2, S^1)$: out-of-plane (OP) [3] and Takeno–Homma (TH) [4] solitons; and to the group $\pi_1(S^1)$: Kosterlitz–Thouless (KT) vortices. They correspond to a map of a spin order parameter space onto a sphere S^2 homeomorphic to the 2D plane or a circle S^1 [5].

In this paper, we use another method of searching for nontrivial topological excitations. By starting from the nonlinear equations for (θ, φ) fields describing the dynamics of a classical 2D isotropic Heisenberg magnet of a spin S with an exchange J [6]

$$0 = \hbar S \sin\theta \frac{\partial \phi}{\partial t} + JS^2(\Delta\theta - \cos\theta \sin\theta (\nabla\phi)^2), \quad (1)$$

$$0 = \hbar S \frac{\partial \theta}{\partial t} + JS^2(2\cos\theta(\nabla\phi\nabla\theta) + \sin\theta\Delta\phi), \quad (2)$$

one can see that, in the stationary case, the field variable θ is determined by only the gradient field $\boldsymbol{\psi} = \nabla\phi$. The Euclidean 2D plane is homeomorphic to the sphere S^2 with one punctured point. According to the Hopf theorem [7], the Eulerian characteristic of a triangulated surface is equal to the sum of indices of singular points of the vector field on the surface. The Eulerian characteristic of the sphere is equal to 2. In the simplest case, one may suggest that one singular point with the Poincaré index +1 is placed at the south pole and the other one at infinity, with the same index corresponding to the punctured point at the north pole. The space configuration of the θ field will depend on the kind of singular point of ψ: a center, a node, or a focus. The center singularity (Fig. 1a) corresponds to the solution of Eq. (2) $\Delta\phi = 0$, and the particular solution $\phi = q\tan^{-1}(y/x)$ results in the well-known solitons with the axial symmetry listed above. One may expect that the focus singularity (Fig. 1b) will correspond to a spiral spin arrangement [8].

The investigation of the paper is devoted to the nodal point of the vector field $\boldsymbol{\psi}$ (Fig. 1c), where $\boldsymbol{\psi}$ has a maximal (minimal) value. This means the choice of the parametrization $\phi = \phi(r)$; i.e., the azimuthal angle changes along the radial direction in the plane. From equation (2), one obtains

$$\frac{d\varphi}{dr} = \frac{q}{r\sin^2\theta}, \quad (3)$$

which determines the radial dependence of the φ field

$$\varphi(r) = \varphi_0 + q\int_a^r \frac{dr'}{r'\sin^2\theta}, \quad (4)$$

where the notation a is used for the lattice unit; φ_0 is an initial value. The equation for the θ angle

$$\Delta\theta - \frac{\cos\theta}{\sin^3\theta}\frac{q^2}{r^2} = 0 \quad (5)$$

may be integrated exactly and results in the scale-invariant solution

$$\theta(r) = \cos^{-1}[\sqrt{1-(q/Q)^2}\sin(p\log[(r/R)^{|Q|}])], \quad p = \pm 1. \quad (6)$$

This represents annuluses logarithmically divergent from the center (Fig. 2) and looks like a "target" with annular domains of magnetization. The parameter $Q^2 \geq q^2$ governs the amplitude of the oscillations, R is a scale factor, and the sign p is the polarity of the solution. The

¶This article was submitted by the authors in English.

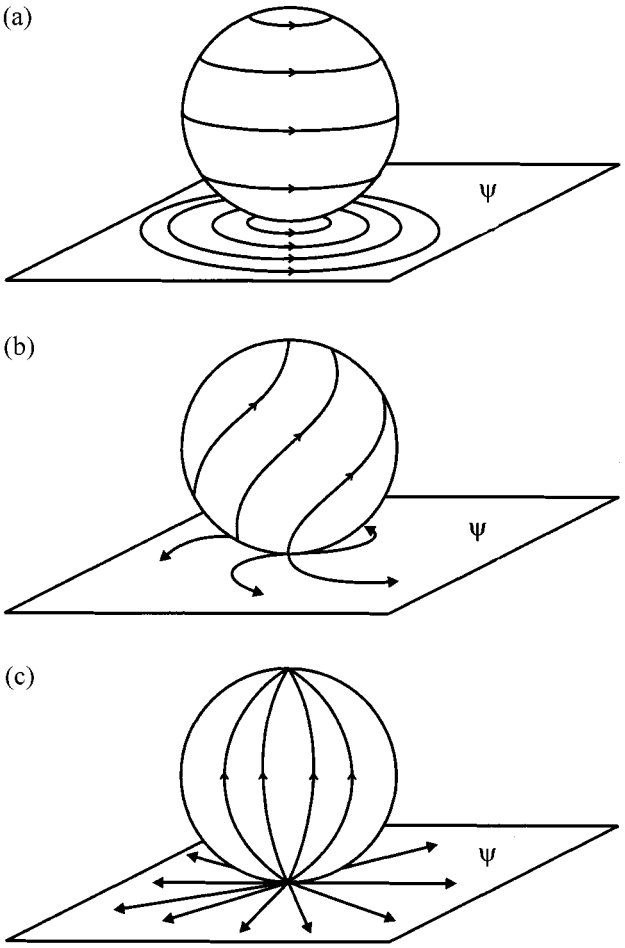

Fig. 1. The types of vector-field singular points on the sphere: (a) center, (b) focus, and (c) node.

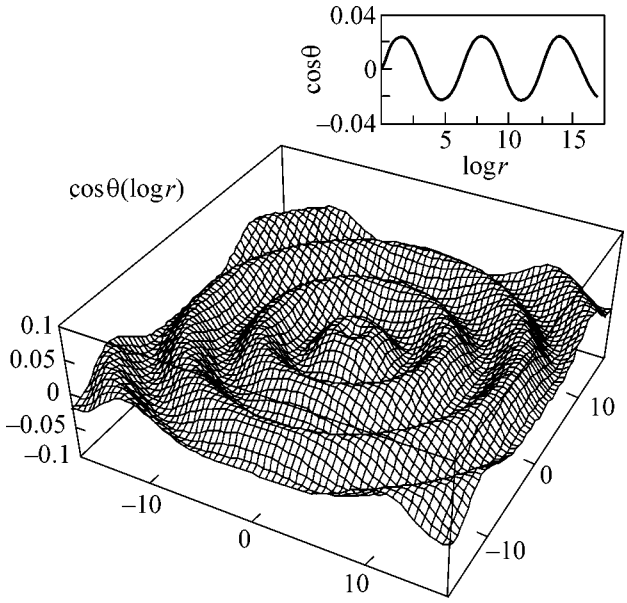

Fig. 2. The space magnetization distribution in the "target." The logarithmic scale is used. The inset shows a radial section of the plot.

continuum description is valid just for distances greater than the lattice unit a, and the R value determines the boundary value $\theta_0 = \theta|_{r=a}$. As is seen from Eq. (6), θ cannot take the values 0 and π. The plane chirality is determined by the sign of parameter q; the corresponding in-plane spin texture is presented in Fig. 3.

This solution is a counterpart of the BP soliton, because it has no definite localization radius and it is scale-invariant. In contrast to the BP soliton, the energy of the found solution

$$E = \frac{JS^2}{2}\int_a^L \left[(\nabla\theta)^2 + \frac{q^2}{r^2\sin^2\theta}\right]d\mathbf{r} = \pi JS^2Q^2\log\left(\frac{L}{a}\right) \quad (7)$$

has no finite value and shows KT logarithmic behavior with an increase of the system size L.

The availability of a pair of stationary solutions resembles somewhat the existence of a fundamental system of linear second-order differential equations. In the study of topological excitations in the classical XY model, we deal with the last situation: in [9], just one of the harmonic functions $\phi = q\tan^{-1}(y/x)$ was considered as physically reasonable; another solution $\bar{\phi} = -q\log r$ was exploited to obtain an effective interaction between vortices.

As follows from Eq. (6), the choice $|Q| = q$ realizes a pure in-plane arrangement $\theta = \pi/2$ and ensures a minimal energy E in the class of solutions. In the logarithmic scale $x = \log(r/R)$, the parameter Q determines the wavelength $\delta = 2\pi/|Q|$, i.e., the distance between the nearest "crests" of the "target." The change of the angle φ on the scale δ is $\Delta\varphi = q\delta$, which leads to the important relation for the small amplitude of the magnetization oscillations ($q \approx Q$)

$$\frac{\Delta\varphi}{2\pi} \approx \frac{q}{|Q|}, \quad (8)$$

i.e., the ratio $q/|Q|$ corresponds to the relative change of the azimuthal angle on the scale δ.

The criterion of topological stability of the BP soliton is rather simple [2]: there is an integer-valued topological invariant Q (degree of the map $S^2 \longrightarrow S^2$) associated with the BP solution $\theta(\mathbf{r})$, $\phi(\mathbf{r})$ via

$$Q = \frac{1}{4\pi}\int \sin\theta(\mathbf{r})d\theta(\mathbf{r})d\phi(\mathbf{r}).$$

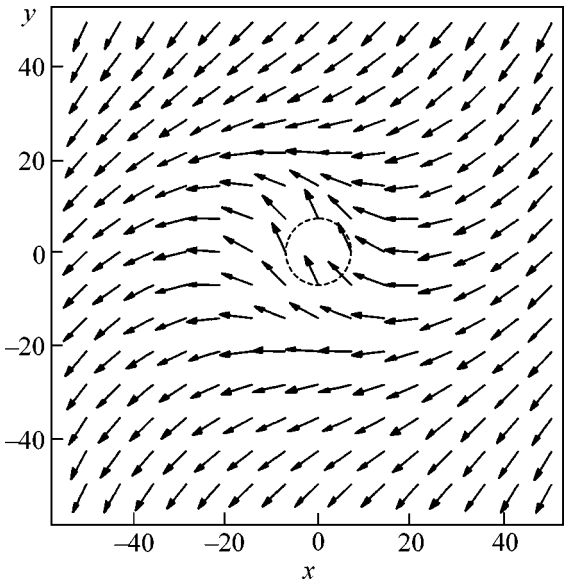

Fig. 3. In-plane spin arrangement of a nodal singularity. The dotted circle displays spin directions at equal distances from the center.

For the soliton with an axial symmetry $\phi = \phi(\alpha)$ (α is the angular polar variable), the topological invariant

$$Q = \frac{\nu}{2}[\cos\theta(0) - \cos\theta(\infty)] = \pm\nu,$$

where ν is a winding number. This describes the change of the ϕ angle when moving around the center $r = 0$,

$$\delta\phi = 2\pi\nu,$$

and is equal to the degree of the map $S^1 \longrightarrow S^1$. A nonzero density of the angular momenta [10]

$$L_z = \nu\hbar S(1 - \cos\theta)$$

and a zero value of the radial part of the momentum density $P_r = 0$ is a common point of the solitons with the center singularity: BP and easy-axis solitons, the OP and TH solitons, and also KT vortices. Thus, the winding number is associated uniquely with the angular-momentum density of the magnetization field.

For the solutions with a nodal singularity, the situation is the opposite: $L_z = 0$ and P_r has the nonzero value [10]

$$P_r = \hbar S(1 - \cos\theta)\frac{d\phi}{dr} = \hbar\frac{qS}{r}\frac{1}{1 + \cos\theta}.$$

For a pure in-plane spin arrangement, the q value determines the scaling factor

$$\log\lambda = \frac{2\pi}{q},$$

such that a change of the azimuthal angle on the scale λ

$$\phi(\lambda r) - \phi(r) = 2\pi.$$

As is seen, the q value is associated identically with the momentum density of the magnetization field.

A special kind of nodal time-dependent solution of the 2D Heisenberg model was considered in [11] by means of the inverse scattering transform. Keeping time-dependent terms in Eqs. (1) and (2), one may obtain solutions with a finite energy and finite localization radius. The radial behavior of the angle variables differs form the situation considered above; for example, θ reveals an exponential dependence at large distances in a fixed time. The solitons are ring-shaped waves. Their localization radius and thickness grows with time linearly, whereas the amplitude is inversely proportional to the time.

It is well known that an exchange anisotropy along the z axis $J_z > J_\perp$ changes its asymptotic behavior at large distances from the power law, decreases to exponential behavior, and results in the easy-axis solitons. An analogous effect occurs in the considered case but only for the plane exchange anisotropy $J_\perp > J_z$. The static equations for the case with an account of an external magnetic field along the z axis h may be written as

$$\begin{aligned} 0 &= J_\perp(4\cos\theta\sin\theta + \cos^2\theta\Delta\theta) \\ &- J_\perp\cos\theta\sin\theta((\nabla\theta)^2 + (\nabla\phi)^2) - 4J_z\cos\theta\sin\theta \\ &+ J_z\cos\theta\sin\theta(\nabla\theta)^2 + J_z\sin^2\theta\Delta\theta - \frac{h}{S}\sin\theta, \end{aligned} \quad (9)$$

$$0 = \sin\theta\Delta\phi + 2\cos\theta(\nabla\theta\nabla\phi). \quad (10)$$

Equation (10) is the same as in the isotropic case and results in relation (4). An analysis of the asymptotic behavior at infinity yields the boundary value

$$\cos\theta_0 = \frac{h}{4S(J_\perp - J_z)}, \quad (11)$$

from which one obtains $\theta_0 = \pi/2$ at $h = 0$, and there are no static solutions at $h \neq 0$ and $J_\perp = J_z$. However, in the last case, there is a dynamic solution $\varphi = \varphi(r) + \omega t$ with the Larmor resonance frequency.

For zero magnetic field h, the asymptotic behavior at $r \longrightarrow \infty$

$$\theta = \frac{\pi}{2} + \delta\theta$$

may be obtained from the equation

$$r^2\frac{d^2\delta\theta}{dr^2} + r\frac{d\delta\theta}{dr} - \left(4\frac{(J_\perp - J_z)}{J_z}r^2 - \frac{J_\perp}{J_z}q^2\right)\delta\theta = 0. \quad (12)$$

The solution is the McDonald's function $\delta\theta = K_\nu(r/\lambda)$, $\nu = iq\sqrt{J_\perp/J_z}$ with the localization radius

$$\lambda = \frac{1}{2}\sqrt{\frac{J_z}{J_\perp - J_z}}. \quad (13)$$

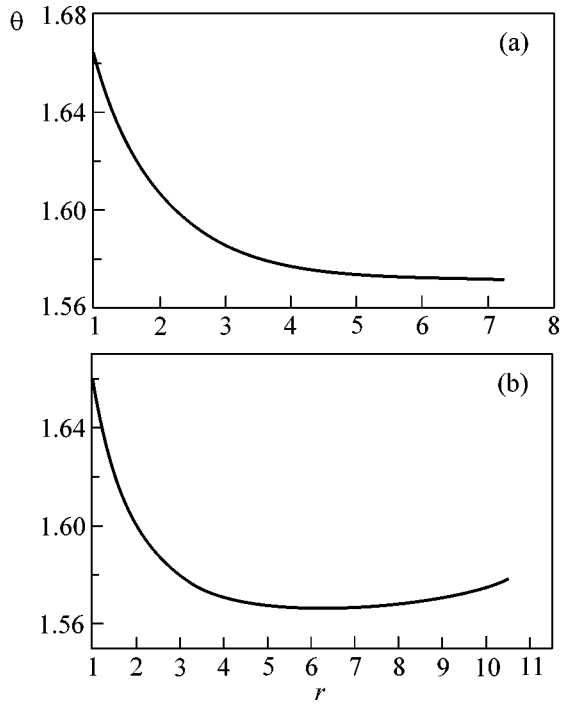

Fig. 4. The θ(*r*) dependence in the (a) nodal out-of-plane and (b) Takeno–Homma soliton.

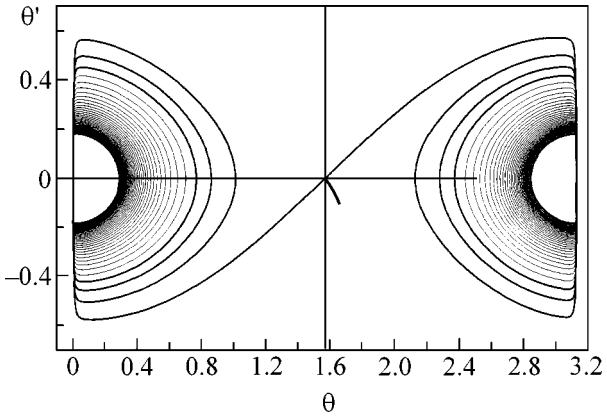

Fig. 5. The phase trajectories of possible solutions of Eq. (9).

The series expansion of solution (6) near the point $r = a$ is

$$\theta(r) \approx \theta(a) + \theta'(a)r. \quad (14)$$

A numerical calculation of Eqs. (9) and (10) is made by the shooting method, and an example of the nodal OP soliton is presented in Fig. 4a. The phase portrait of possible behavior of the solutions is presented in Fig. 5. An arbitrary choice of the derivative θ'(*a*) results in energetically unfavorable oscillating solutions above or below $\theta = \pi/2$ (left and right limit cycles), and only a unique choice of the derivative gives the soliton. As in the case of the conventional OP with an axial symmetry, the energy has a logarithmic divergence with growing soliton size.

Finally, we point out that inclusion of the external magnetic field *h* changes the asymptotic behavior of the soliton at infinity from the exponential into the power decay

$$\delta\theta \approx -\frac{1}{4}\frac{J_\perp}{J_\perp - J_z}\frac{\cos\theta_0}{\sin^5\theta_0}\frac{q^2}{r^2}, \quad (15)$$

where q_0 is given by (11). This is a counterpart of conventional TH solitons (Fig. 4b).

In conclusion, the class of nodal stationary states in the 2D Heisenberg model is investigated. The scale-invariant solution, a counterpart of the BP soliton, is found. An account of in-plane exchange anisotropy yields the analogues of out-of-plane and Takeno–Homma solitons; however, in contrast to the conventional solutions, those which are considered in the paper have no axial symmetry.

This work was partially supported by the US CRDF (grant no. NREC-005), by INTAS (grant no. 01-0654), and by the Program "Russian Universities" (grant no. UR.01.01.005).

REFERENCES

1. A. A. Belavin and A. M. Polyakov, Pis'ma Zh. Éksp. Teor. Fiz. **22**, 503 (1975) [JETP Lett. **22**, 245 (1975)].
2. A. M. Kosevich, B. A. Ivanov, and A. S. Kovalev, Phys. Rep. **194**, 119 (1990); A. S. Kovalev, A. M. Kosevich, and K. V. Maslov, Pis'ma Zh. Éksp. Teor. Fiz. **30**, 321 (1979) [JETP Lett. **30**, 296 (1979)].
3. M. E. Gouvea, G. M. Wysin, A. R. Bishop, and F. G. Mertens, Phys. Rev. B **39**, 11840 (1989).
4. S. Takeno and S. Homma, Prog. Theor. Phys. **65**, 172 (1981).
5. N. D. Mermin, Rev. Mod. Phys. **51**, 591 (1979).
6. R. Balakrishnan and A. R. Bishop, Phys. Rev. B **40**, 9194 (1989).
7. B. A. Dubrovin, A. T. Fomenko, and S. P. Novikov, *Modern Geometry—Methods and Applications*, Part 2: *The Geometry and Topology of Manifolds* (Springer, New York, 1985).
8. A. B. Borisov, Pis'ma Zh. Éksp. Teor. Fiz. **73**, 279 (2001) [JETP Lett. **73**, 242 (2001)].
9. J. M. Kosterlitz, J. Phys. C: Solid State Phys. **7**, 1046 (1974).
10. R. F. Egorov, I. G. Bostrem, and A. S. Ovchinnikov, Phys. Lett. A **292**, 325 (2002).
11. A. V. Mikhaĭlov and A. I. Yaremchuk, Pis'ma Zh. Éksp. Teor. Fiz. **36**, 78 (1982) [JETP Lett. **36**, 95 (1982)].

JETP Letters, Vol. 76, No. 12, 2002, pp. 720–723. Translated from Pis'ma v Zhurnal Éksperimental'noĭ i Teoreticheskoĭ Fiziki, Vol. 76, No. 12, 2002, pp. 850–854.

Coulomb Blockade in a Lateral Triangular Small Quantum Dot

V. A. Tkachenko[1, *], Z. D. Kvon[1], O. A. Tkachenko[1], D. G. Baksheev[1], O. Estibals[2], and J. C. Portal[2]

[1] *Institute of Semiconductor Physics, Siberian Division, Russian Academy of Sciences, Novosibirsk, 630090 Russia*
**e-mail: vtkach@isp.nsc.ru*
[2] *Grenoble High Magnetic Fields Laboratory, MPI-FKF and CNRS, B.P.166, F-38042 Grenoble, France*
Received November 27, 2002

An AlGaAs/GaAs lateral quantum dot of triangular shape with a characteristic size $L < 100$ nm (the smallest size for dots of this type) containing less than ten electrons was studied theoretically and experimentally. Single-electron oscillations of the conductance G of this dot were measured at $G < e^2/h$. When going from $G \ll e^2/h$ to $G \approx 0.5e^2/h$, a decrease was found not only in the amplitude but also in the period of oscillations. A calculation of the electrostatics demonstrated that this effect is due to a change in the dot size produced by control voltages. © *2002 MAIK "Nauka/Interperiodica".*

PACS numbers: 73.21.La; 73.23.Hk; 73.50.-h

Lateral submicron quantum dots have been the main object for studying Coulomb blockade effects and related phenomena for more than ten years [1–3]. Commonly, these dots contain ~100 electrons. Currently, the problem associated with creating and studying small lateral dots has gained special importance. This is caused by the fact that two tunnel-coupled dots each containing one electron represent one of the attracting systems for detecting entangled quantum states [4–6]. However, until recently, real lateral quantum dots have contained more than ten electrons [6–8] and had a characteristic size $L > 100$ nm.

This work reports the properties of a lateral quantum dot, whose area and capacity can be minimized because of its triangular shape. The main parameters of the quantum dot were found from modeling the three-dimensional electrostatics of the device with regard to the special features of its fabrication (the structure of the initial heterojunction, the etching depth, the presence of the upper metallic gate, etc.). Coulomb blockade effects were studied experimentally, and a comparative analysis of the behavior of single-electron oscillations and the results of modeling was performed. It was shown that a lateral quantum dot with a small ($N < 10$) number of electrons could be created even with the use of intermediate-resolution electron lithography.

Quantum dots studied in this work were fabricated on the basis of a high-mobility two-dimensional electron gas (2DEG) in an AlGaAs/GaAs heterojunction with a mobility $\mu = 3 \times 10^5$ cm^2 V^{-1} s^{-1} and an electron concentration $n = 3 \times 10^{11}$ cm^{-2}. The procedure of their manufacturing was as follows. Three antidots located at the vertices of an equilateral triangle and the insulating grooves were created by electron lithography followed by plasma-chemical etching. The distance between the antidot centers was $d = 0.4$ μm, and their lithographic diameter was $a = 0.2$ μm. A microphotograph of the junction made after the indicated technological procedures is presented in Fig. 1a. Sputtering the continuous metallic TiAu gate was the final step. A schematic section of the junction with an indication of the corresponding sizes and parameters (layer thicknesses, doping level, etch depth) is shown in Fig. 1b. The potential was calculated by numerically solving the three-dimensional Poisson equation. The computational method is described in [9]. As distinct from the indicated work, we used the condition of Fermi level mid-gap pinning at the heteroboundary with the GaAs substrate. We also assumed that the charge of the doping impurities remained constant under nonequilibrium conditions and took into account the effect of impurity potential fluctuations.

The calculated results are shown in Fig. 2 as a 2D electron density distribution in the 2DEG plane. Consider first this distribution under the assumption that the charge density is uniform in delta-doped layers and at zero voltage at the upper gate ($V_g = 0$). A quantum dot approximately triangular in shape is clearly seen in Fig. 2a. It is formed by the boundaries of the depletion regions around antidots. The three vertices of this "triangle" represent saddle points through which the quantum dot is connected with the corresponding 2D reservoirs. In the case under consideration, the dot is open: the Fermi level lies above the bottom of conduction band at the points of narrowing. The area of the quantum dot is small even in this state: $S \approx (6–8) \times 10^{-11}$ cm^2, and the maximum electron concentration (at the dot center) turns out to be considerably (one and a half times) lower than in the initial 2DEG and rapidly decreases toward the dot boundaries. It is evident that the contours of increased density have an ideal triangu-

lar shape. The number of electrons inside these contours can be estimated at $N = 10–15$, and the total number of electrons equals 20–25. Thus, the quantum dot created by the proposed method has a small size and contains a small number of electrons even at $V_g = 0$. However, the boundaries of the quantum dot in the open state are rather conventional. Let us analyze the situation where the dot is brought to the closed regime suitable for the observation of Coulomb blockade effects. The pattern of electron density distribution for one of the closed dot states ($V_g = –150$ mV) is shown in Fig. 2b. The negative potential at the upper gate extends the depletion regions and reduces the electron concentration. The closed state means that the Fermi level lies very close to or even lower than the saddle points of the potential and the quantum dot boundaries are well defined. As compared to the open state, the area of the triangular dot becomes significantly smaller, and the total number of electrons in the dot decreases down to $N \approx 8$.

Figures 2a and 2b show that, if the quantum dot is symmetric with respect to the vertical line, it is more strongly connected with the lower reservoir than with the lateral ones. In fact, technological tolerances and the fluctuation potential distort the ideal shape of the triangular dot and saddle potentials. This may lead to a wide scatter of resistances of three 2D reservoir–dot input/output ports and also to a decrease in the number of electrons in the dot. This situation is shown in Fig. 2c for $V_g = 0$. It is evident that one of the input/output ports turns out to be closed, whereas the remaining two are open and have different resistances. Here, the total number of electrons in the dot decreased by one half. This property of the junctions was used in the experiment to design a small single-electron transistor. The highest resistance input/output port to the dot in this transistor was used as a side control gate changing the number of electrons in the dot, and the upper metal gate was used for measuring the resistance of the remaining two input/output ports. The schematic diagram of measurements is given in Fig. 3. Numbers *1* and *2* in this figure indicate the input/output ports through which the double-dot conductance of the dot G_{1212} was measured, and number *3* marks the input/output port through which the side gate voltage V_{jg} was applied. The measurements were performed at a temperature of 50 mK on the basis of a four-probe circuit at a frequency of 7.5 Hz and currents of 0.1–1 nA.

The experimental results are presented in Fig. 4. The conductance G_{1212} of the dot is shown in Fig. 4a as a function of V_{jg} for various upper gate voltages V_g and, respectively, for various conductances in the closed state. It is clear that the corresponding curves represent oscillations equidistant in V_{jg}, which is characteristic of transistor structures which operate on the basis of the Coulomb blockade effect. Thus, each oscillation is associated with one electron added to or removed from the dot. Note that, as distinct from the dots studied previously in [3–5], the single-electron oscillations observed in this work are not shaped at $G \ll e^2/h$ as deltalike peaks with wide regions of almost zero conductance but have a shape close to sinusoidal. This may be connected with the fact that one of the input ports to the dot, for example, the second in Fig. 3, is almost open. In order to check this hypothesis, we enhanced the coupling of the dot to 2D reservoirs. The dependence $G_{1212}(V_{jg})$ is shown in Fig. 4b for $V_g = –50$ mV and –60 mV. It is clearly seen that the background conductance increased up to values $G \approx 0.5e^2/h$ and the oscillations behave differently. First, the conductance exhibits a minimum at zero displacement V_{jg} ($V_g = –50$ mV) and at $V_{jg} = –10$ mV ($V_g = –60$ mV). Second, almost complete suppression of Coulomb oscillations is observed. The first effect can be associated with the influence of lateral displacement on the barrier height, because the barrier height is already sufficiently small in the described state. The second and more important effect was observed previously in [10] for large quantum dots. This effect is associated with the suppression of the Coulomb blockade when the dot passes from the closed ($G \ll e^2/h$) to the open ($G > e^2/h$) state.

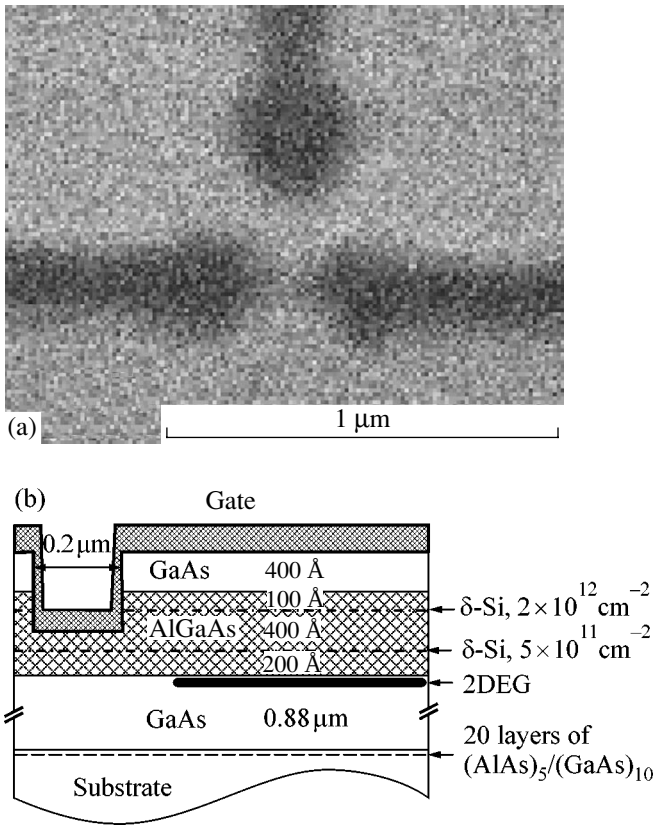

Fig. 1. (a) Scanning electron microscope image of the structure. (b) Schematic cross section of the initial heterojunction.

A comparison of Figs. 4a and 4b shows that, along with a sharp decrease in the amplitude of single-elec-

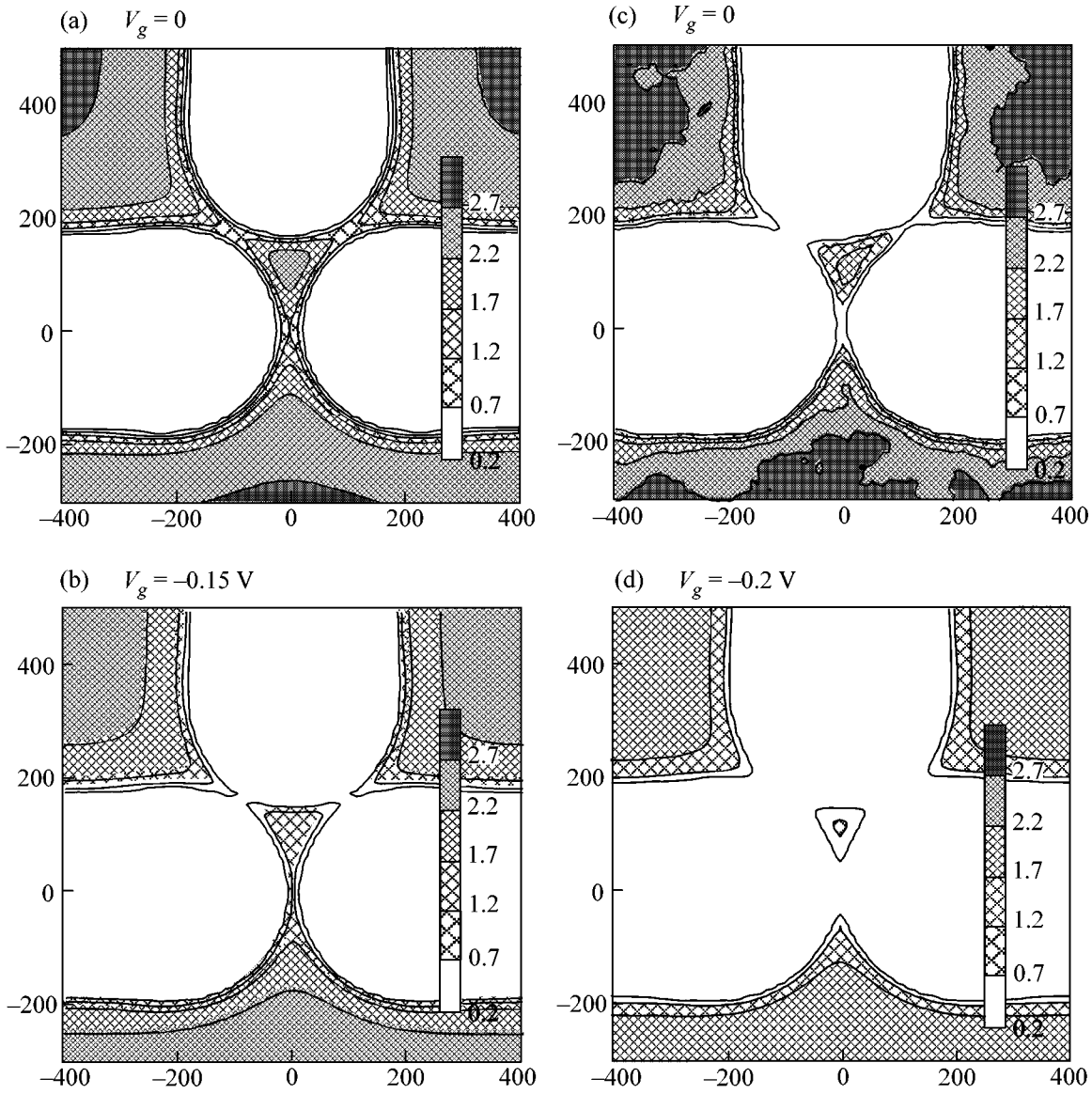

Fig. 2. Electron density contour maps $n[10^{-3}\ \mathrm{nm}^{-2}]$ for (a, c) open and (b, d) closed triangular quantum dots. (c) Result of the influence of the fluctuation potential of the delta-doped layers. (d) State of a dot with two electrons and a conductance of $<10^{-10}\ e^2/h$ (tunnel barriers have a height of >10 meV and a width of 150 nm).

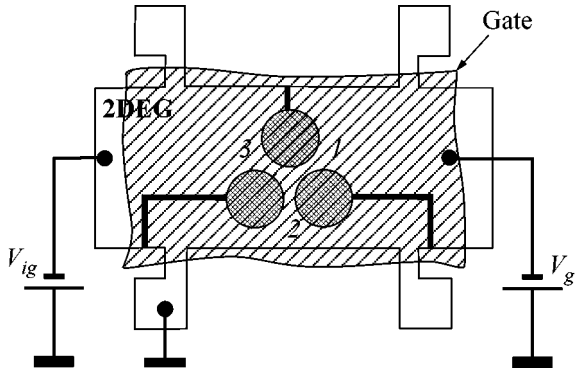

Fig. 3. Schematic diagram of a Hall bridge with a single-electron transistor based on a triangular quantum dot.

tron oscillations, a decrease in their period relative to the side gate is also observed. The decrease in the period can be connected with the fact that, because of the smallness of this dot, the change in its state produced by the control gate voltages also leads to a notable change in its size (Fig. 2). To compare the calculated and experimental data more accurately, we calculated the capacity C_{jg} between the 2D reservoir and the dot as a function of the upper gate voltage. The calculated value of e/C_{jg} for the closed state equals 18–20 mV at $V_g = -150$ mV, which is in a good agreement with the measured period of conductance oscillations in Fig. 4a. The calculated results also predict a decrease in e/C_{jg} to 14–15 mV at a voltage $V_g = -75$ mV, which cor-

responds in the model to the transition to the open state of the dot. Oscillations with this period are seen in Fig. 4b. Such an agreement between calculation and experiment indicates that the computer model of the nanostructure studied in this work quite adequately reflects its properties.

The model constructed indicates that single-electron oscillations must terminate in the region $V_g \sim -120 \ldots -220$ mV, because both the tunnel conductance and the number of electrons decrease almost to zero (Fig. 2d). This prediction is confirmed by the experimental behavior of Coulomb oscillations. The positive sign in the $G_{1212}(V_{jg})$ curves corresponds to the addition of electrons to the dot, and the negative sign corresponds to their removal. An analysis of the $G_{1212}(V_{jg})$ curves (Fig. 4a) in the vicinity of the lowest V_g values demonstrates that a relative symmetry in the behavior of $G_{1212}(V_{jg})$ is observed upon passing through the point $V_{jg} = 0$ at $V_g > -120$ mV. The appearance of new peaks at $V_{jg} < 0$ is clearly seen. On the other hand, a sharp asymmetry is observed in the $G_{1212}(V_{jg}, V_g = -120$ mV) curve: at $V_{jg} < 0$ no conductance peaks are observed, and $G \longrightarrow 0$. It should be noted that the threshold voltages strongly depend on the uncontrolled factors like the charge of doping impurities and states at the AlGaAs/GaAs surface exposed to plasma-chemical etching. For example, if the capacity of these states and the fluctuation potential are neglected, the single-electron state of the dot is at the boundary of the experimental range $V_g = -120$ mV. Quite the reverse, if this capacity is very large, the charging of the introduced surface states fully screens a change in the voltage V_g at the metal covering the etched areas. The results of modeling discussed above are related just to this case, and at $V_g = -220$ mV the dot in this case has one electron. The fluctuation potential can shift the thresholds toward the experimental range, because the fluctuation amplitude ~1 meV is comparable with the potential-well depth in the quantum dot. With regard to the uncertainty $\Delta V_g \sim$ 100 mV noted above, the calculated position of the single-electron state of the dot is in a reasonable agreement with the measured oscillation disappearance threshold. However, the facts presented above do not allow us to assert that a single-electron state of the dot is achieved in the experiment, because the asymmetry of the $G_{1212}(V_{jg})$ dependence at $V_g = -120$ mV mentioned above can be associated with a sharp decrease in the potential barrier between the dot and the 2D reservoir (Figs. 2b, 2d).

Thus, the results of this work indicate that a single-electron transistor is realized in a lateral triangular small dot with a few electrons. It is shown by calculations that a single-electron state can be obtained in a quantum dot based on 2DEG in an AlGaAs/GaAs heterojunction.

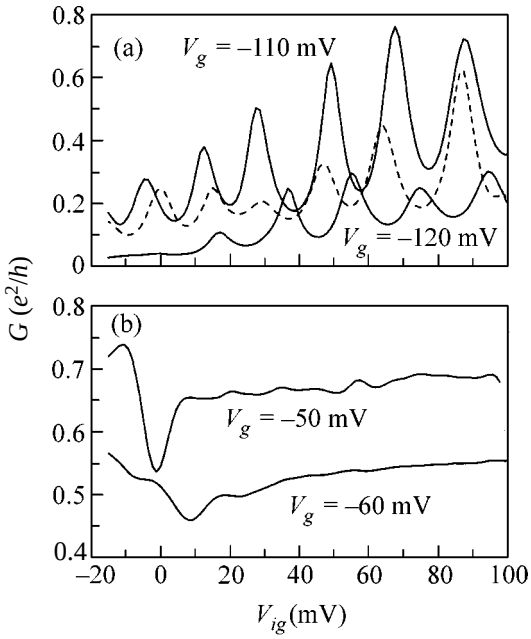

Fig. 4. Dependence of the conductance $G_{1212}(V_{jg})$ at various upper gate voltages V_g: (a) well-defined and (b) suppressed Coulomb oscillations ($V_g = -115$ mV for the dashed curve).

This work was supported by the Russian Foundation for Basic Research, project no. 16516, the Ministry of Science, programs "Physical Fundamentals of Quantum Computations and Telecommunications" and "Physics of Solid-State Nanostructures," INTAS, project no. 01-0014, and the Russian Academy of Sciences, programs "Quantum Macrophysics" and "Low-Dimensional Quantum Structures."

REFERENCES

1. K. K. Likharev, IBM J. Res. Dev. **32**, 144 (1988).
2. L. I. Glazman and R. I. Shekhter, J. Phys.: Condens. Matter **1**, 5811 (1989).
3. M. A. Kastner, Rev. Mod. Phys. **64**, 849 (1992).
4. D. Loss and D. P. DiVincenzo, Phys. Rev. A **57**, 120 (1998).
5. D. Loss and E. Sukhorukov, Phys. Rev. Lett. **84**, 1035 (2000).
6. A. W. Holleitner, C. R. Decker, H. Qin, *et al.*, Phys. Rev. Lett. **87**, 256802 (2001).
7. D. S. Duncun *et al.*, Appl. Phys. Lett. **77**, 2183 (2000).
8. V. Zozoulenko, A. S. Sachrajda, C. Gould, *et al.*, Phys. Rev. Lett. **83**, 1838 (1999).
9. O. A. Tkachenko, V. A. Tkachenko, D. G. Baksheev, *et al.*, Pis'ma Zh. Éksp. Teor. Fiz. **71**, 366 (2000) [JETP Lett. **71**, 255 (2000)].
10. A. Pasquier, U. Meirav, F. I. B. Williams, *et al.*, Phys. Rev. Lett. **70**, 69 (1993).

Translated by A. Bagatur'yants

JETP Letters, Vol. 76, No. 12, 2002, pp. 724–727. From Pis'ma v Zhurnal Éksperimental'noĭ i Teoreticheskoĭ Fiziki, Vol. 76, No. 12, 2002, pp. 855–858.

Anticommutativity Equation in Topological Quantum Mechanics¶

V. Lysov

Institute of Theoretical and Experimental Physics, Moscow, 117259 Russia
Moscow Institute of Physics and Technology, Moscow, 141700 Russia
e-mail: sllys@gate.itep.ru

Received November 21, 2002

We consider topological quantum mechanics as an example of topological field theory and show that its special properties lead to numerous interesting relations for topological correlators in this theory. We prove that the generating function $\mathcal{F}$ for these correlators satisfies the anticommutativity equation $(\mathcal{D} - \mathcal{F})^2 = 0$. We show that the commutativity equation $[dB, dB] = 0$ can be considered as a special case of the anticommutativity equation.
© 2002 MAIK "Nauka/Interperiodica".

PACS numbers: 03.65.Ca; 02.40.Vh

1. During the last two decades, there has been much interest in quantum field theories whose correlators do not depend on points and metric but only on the topology of the manifold and on the types of operators in the correlators. These theories are called topological [1]. Among the most celebrated examples are the Chern–Simons theory [2], $N = 2$ twisted gauge theories [3], and topological sigma models [4]. Here, we consider yet another, much simpler example of topological theory, which is a subsector of supersymmetric quantum mechanics. We call it topological quantum mechanics.

An explicit construction of many topological theories is given by a BRST-like symmetry operator Q, $Q^2 = 0$, so that the energy–momentum tensor of the theory has the special form [3]

$$T_{\mu\nu} = \{Q, G_{\mu\nu}\}, \tag{1}$$

where $G_{\mu\nu}$ is some tensor. This formula leads to many interesting corollaries. In particular, it provides correlators with the independence of metric and points, which are topological invariants.

In the case of one-dimensional theory, the energy–momentum tensor has only one component and is equal to the Hamiltonian

$$H = T_{00} = \{Q, G_{00}\} = \{Q, G_+\}. \tag{2}$$

In topological quantum mechanics, the objects of study are correlators $\langle \Phi_{A_1}(t_1)\dots\Phi_{A_n}(t_n)\rangle$ of Q-closed operators. They would seem to depend on n times $t_1 < \dots < t_n$. However, since the energy–momentum tensor is the anticommutator of Q and G_+, the correlator actually does not depend on t and is given by the factorization formula

$$\begin{aligned}
&\langle \Phi_{A_1}(t_1)\dots\Phi_{A_n}(t_n)\rangle \\
&= \left\langle 0\middle| e^{-t_1 H}\Phi_{A_1} e^{(t_1-t_2)H}\Phi_{A_2}\dots e^{(t_{n-1}-t_n)H}\Phi_{A_n}e^{t_n H}\middle|0\right\rangle \\
&= \lim_{(t_k - t_{k-1})\to\infty}\left\langle 0\middle|\Phi_{A_1} e^{(t_1-t_2)H}\dots e^{(t_{n-1}-t_n)H}\Phi_{A_n}\middle|0\right\rangle \\
&= \langle\Phi_{A_1}\rangle\dots\langle\Phi_{A_n}\rangle.
\end{aligned} \tag{3}$$

This means that it is sufficient to study the correlators of one operator Φ_A in the theory with the deformed supercharge Q:

$$Q \longrightarrow Q + \sum \Phi_A T_A = Q + \Phi. \tag{4}$$

Later, we will see that this one-point correlator is a total derivative of $\mathcal{F}$ on the space of coupling constants T_A:

$$\partial_A \mathcal{F} = \langle\Phi_A\rangle_{\text{deformed}} = \langle T\{\Phi_A e^{\int\{\Phi, G_+\}dt}\}\rangle, \tag{5}$$

where $T\{\dots\}$ stands for the chronological ordering. In what follows, we carefully formulate the theory and realize that the function $\mathcal{F}$ satisfies an interesting quadratic differential equation, which we call the anticommutativity equation.

2. Thus, we consider the simplest example of topological field theory: topological quantum mechanics. As usual, there is a nilpotent symmetry operator Q, and one can introduce the Hamiltonian in the form (2). All the operators act on the space V with the following properties:

$$\begin{gathered}
V = V_1 \oplus V_0, \\
HV_0 = 0, \quad QV_0 = 0, \\
H > 0 \text{ on } V_1.
\end{gathered} \tag{6}$$

¶This article was submitted by the author in English.

This physically means that V is the state space of our system and V_0 is the vacuum-state space. We assume that the kernel V_0 of the Hamiltonian consists of Q-closed states and that all nonzero energies have a strictly positive real part. In this theory, we study correlators of the form (5), which are vacuum matrix elements, i.e., the operators from Hom(V_0, V_0), and which can be written in the following form:[1]

$$\begin{aligned} &F^{(k)}_{\alpha\beta} \\ &= \int_0^\infty \dots \int_0^\infty \left\langle 0_\alpha \middle| \Phi G_+ e^{-t_1 H} \Phi G_+ e^{-t_2 H} \dots \Phi \middle| 0_\beta \right\rangle dt_1 \dots dt_{k-1} \\ &= \frac{1}{k!} \left\langle T\left\{ \Phi(0) \left(\int_{-\infty}^{+\infty} \{G_+, \Phi(t) dt\} \right)^{k-1} \right\} \right\rangle_{\alpha\beta}. \end{aligned} \tag{7}$$

We want to present this operator from Hom(V_0, V_0) as an operator from Hom(V, V). The way to do this is to insert Π_0's at the beginning and at the end. After this, we finally obtain the object we need:

$$\begin{aligned} &\mathcal{F}^{(k)} \\ &= \int_0^\infty \dots \int_0^\infty \Pi_0 \Phi G_+ e^{-t_1 H} \Phi G_+ e^{-t_2 H} \dots \Phi \Pi_0 dt_1 \dots dt_{k-1}. \end{aligned} \tag{8}$$

Here, Φ is the generating function of the operators

$$\Phi = \Phi(0) = \sum \Phi_A T_A. \tag{9}$$

Our theory is Euclidean, which means that the evolution Φ in time can be described by the formula

$$\Phi(t) = e^{-tH} \Phi(0) e^{tH}. \tag{10}$$

Our operators can be both even and odd; therefore, we need to introduce a superalgebra for describing their properties, our coupling constants T_A being graded too. Their algebra is

$$\{T_A, T_B\}_s = 0, \tag{11}$$

where $\{\dots\}$ stands for the supercommutator.

In order to get some nontrivial interesting properties of the correlators, let us consider a special set of operators that satisfy the algebra

$$\begin{aligned} \{\Phi_A, \Phi_B\}_s &= C^K_{AB} \Phi_K, \\ \{Q, \Phi_A\}_s &= 0. \end{aligned} \tag{12}$$

[1]Here, we used the properties $G_+^2 = 0$ and $G_+ V_0 = 0$, which allow one to interpret F as a correlator in topological theory, but they are not necessary for our main result.

Π_0 being a projector onto the vacuum states. One can rewrite Π_0 in terms of H:

$$\Pi_0 = \lim_{t \to \infty} e^{-tH}. \tag{13}$$

It commutes with Q. Therefore,

$$\begin{aligned} Q\Pi_0 &= \Pi_0 Q = 0, \\ \langle 0_\alpha | Q &= \langle 0_\alpha | \Pi_0 Q = 0. \end{aligned} \tag{14}$$

3. The algebra of operators Φ **generates numerous commutation relations** for $\mathcal{F}^{(k)}$, which can be written in a compact form in terms of the generating function $\mathcal{F}$

$$\mathcal{F} = \sum \mathcal{F}^{(k)} \tag{15}$$

as

$$\{\mathcal{F}, \mathcal{F}\} = T_A T_B C^K_{AB} \partial_K \mathcal{F}. \tag{16}$$

One can easily obtain all our correlators as derivatives of $\mathcal{F}$. We now prove this equation in the generic case.

Let us introduce an operator-valued differential form of indefinite rank on R:

$$U = e^{-tH} + G_+ dt e^{-tH}. \tag{17}$$

We can check that

$$dU + \{Q, U\} = 0. \tag{18}$$

One can construct the differential form on R^{k-1}, which takes a value in Hom(V, V) and includes $k+1$ Φ's

$$\omega^{(k-1)} = \Pi_0 \Phi U_1 \dots \Phi U_k \Phi \Pi_0. \tag{19}$$

Our form is d-closed, because $Q\Pi_0 = \Pi_0 Q = 0$ and Φ anticommutes with Q:

$$\begin{aligned} d\omega^{(k-1)} &= -\Pi_0 \Phi \{U_1, Q\} \dots \Phi U_k \Phi \Pi_0 \\ &- \dots - \Pi_0 \Phi U_1 \dots \Phi \{U_k, Q\} \Phi \Pi_0 = 0. \end{aligned} \tag{20}$$

One can consider the integral of the rank $k-1$ component of our form over the boundary of some surface and rewrite it as an integral of $d\omega^{(k-1)}$ over this surface by the Stokes theorem. The surface of integration is the boundary of a k-dimensional cube. The result of integration is

$$\begin{aligned} &\int_0^\infty \dots \int_0^\infty \Pi_0 \Phi (\Pi_0 - 1) \Phi G_+ e^{-t_1 H} \dots G_+ e^{-t_k H} \\ &\times \Phi \Pi_0 dt_1 \dots dt_{k-1} + (\text{perm. of } \Pi_0 - 1) = 0. \end{aligned} \tag{21}$$

The terms that include Π_0 come from the commutator $\{\mathcal{F}, \mathcal{F}\}$, while other terms come from $T_A T_B C^K_{AB} \partial_K \mathcal{F}$. For our superalgebra of operators Φ_A, one can write (super)Jacobi identities in form

$$C^K_{AB} C^E_{KD} = 0. \tag{22}$$

If we introduce the derivative $\mathcal{D} = \frac{1}{2} T_A T_B C^K_{AB} \partial_K$, our anticommutativity equation can be written as the zero-curvature equation

$$\{\mathcal{D} - \mathcal{F}, \mathcal{D} - \mathcal{F}\} = 0. \quad (23)$$

4. Let us consider what this equation gives for the linear part of $\mathcal{F}$ in (15), F_A. Then, (23) leads to

$$\{F_A, F_B\} = C^K_{AB} F_K. \quad (24)$$

For odd operators Φ_A, this equation is quite nontrivial. One can see this by considering the matrix example. In this case, our state space V is the four-dimensional vector space. The operators Q and G_+ are 4×4 matrices

$$Q = \begin{pmatrix} 0&0&0&0 \\ 1&0&0&0 \\ 0&0&0&0 \\ 0&0&0&0 \end{pmatrix}, \quad G_+ = \begin{pmatrix} 0&1&0&0 \\ 0&0&0&0 \\ 0&0&0&0 \\ 0&0&0&0 \end{pmatrix},$$
$$H = \{Q, G_+\} = \begin{pmatrix} 1&0&0&0 \\ 0&1&0&0 \\ 0&0&0&0 \\ 0&0&0&0 \end{pmatrix}. \quad (25)$$

V_0 is the subspace of V with the first two zero coefficients. The operators Φ_A that satisfy commutation relation (15) are

$$\Phi_A = \begin{pmatrix} a & 0 & 0 & 0 \\ * & -a & * & * \\ * & 0 & & \\ * & 0 & & F_A \end{pmatrix}, \quad (26)$$

where stars are some numbers. When considering commutation relations on Φ_A, we are interested only in the right bottom block. It is easy to show that in this block there is the anticommutator of the two right bottom blocks of Φ_A and Φ_B. This is what we get by commuting matrix elements F_A. This block is the only one remaining after acting of the two projectors onto Φ_A. Thus, we observe that it is only these special commutation relations of matrices Φ_A that provide us with the similar algebra for Φ_A (i.e., for the right bottom blocks)

$$\{\Phi_A, \Phi_B\} = \begin{pmatrix} * & * & * & * \\ * & * & * & * \\ * & * & & \\ * & * & & \{F_A, F_B\} \end{pmatrix}. \quad (27)$$

In the previous formula, one could see that no other block contributes to the right bottom block. Let us see this in terms of operators F_A. Consider

$$\{F_A, F_B\} = \Pi_0 \Phi_A \Pi_0 \Phi_B \Pi_0 + \Pi_0 \Phi_B \Pi_0 \Phi_A \Pi_0. \quad (28)$$

Using formula (13) for the projector, one arrives at the formula

$$\Pi_0 = \lim_{t \to \infty} e^{-tH} = \lim_{t \to \infty} \sum (-t)^k \frac{H^k}{k!} = 1 + \left(\sum Q G_+ (-t)^k \frac{H^{k-1}}{k!} + \sum (-t)^k G_+ \frac{H^{k-1}}{k!} Q \right)\Big|_{t \to \infty}. \quad (29)$$

An important property of this representation is

$$\Pi_0 \Phi_A Q G_+ (-t)^k \frac{H^{k-1}}{k!} \Phi_B \Pi_0 = 0,$$
$$\Pi_0 \Phi_A G_+ (-t)^k \frac{H^{k-1}}{k!} Q \Phi_B \Pi_0 = 0. \quad (30)$$

Hence, the only term in (28) that survives is the c-number term in (29) and

$$\{F_A, F_B\} = \Pi_0 \Phi_A \Phi_B \Pi_0 + \Pi_0 \Phi_B \Phi_A \Pi_0 = C^K_{AB} F_K. \quad (31)$$

5. Our anticommutativity equation contains the commutativity equation introduced in [5–7] as a special case for special operators. Recall the commutativity equations have the form

$$[B_\mu, B_\nu] = 0, \quad B_\mu = \frac{\partial B}{\partial \tau_\mu}. \quad (32)$$

Namely, consider a new odd operator G_- that satisfies

$$G_-^2 = 0, \quad \{G_-, G_+\} = 0,$$
$$\{G_-, Q\} = 0, \quad G_- V_0 = 0. \quad (33)$$

Consider even operators Φ_μ that satisfy relations (12) with $C = 0$ and

$$[[\Phi_\mu, G_-], \Phi_\nu] = 0. \quad (34)$$

These properties allow us to add the new odd operators $\Phi'_\mu = [\Phi_\mu, G_-]$ to our algebra, because they satisfy (12) and have $\mathcal{F}$ in their terms. The main object in commutativity equations in terms $\mathcal{F}$ is

$$B_\mu = \frac{\partial \mathcal{F}}{\partial \theta_\mu}\Big|_{\theta = 0}. \quad (35)$$

Here, we introduce two kinds of coupling constants T_A: even τ_μ and odd θ_μ. One can show that (33) leads to

$$\mathcal{F}|_{\theta = 0} = 0, \quad \text{so}$$
$$\frac{\partial}{\partial \theta_\mu} \frac{\partial}{\partial \theta_\nu} \{\mathcal{F}, \mathcal{F}\}\Big|_{\theta = 0} = [\partial_\mu \mathcal{F}|_{\theta = 0}, \partial_\mu \mathcal{F}|_{\theta = 0}] = 0. \quad (36)$$

This can be the commutativity equation if we show that $B_\mu = \partial B/\partial\tau_\mu$. It follows from the properties of G_- that

$$B_\mu = \frac{\partial B}{\partial\tau_\mu} \longrightarrow \frac{\partial B_\nu}{\partial\tau_\mu} = \frac{\partial B_\mu}{\partial\tau_\nu} \tag{37}$$
$$\sim \ldots\Phi_\mu G_+ e^{-tH}[\Phi_\nu, G_-]\ldots = \ldots[\Phi_\mu, G_-]G_+ e^{-tH}\Phi_\nu\ldots$$

6. Consider the deformation of the solutions for the anticommutativity equation by variation of operator G_+ in terms of $\mathcal{K} = G_+/H = \int_0^\infty G_+ e^{-tH} dt$, so that

$$\{\mathcal{K}, Q\} = 1 - \Pi_0. \tag{38}$$

The variation of $\mathcal{K}$ satisfies

$$\{\delta\mathcal{K}, Q\} = 0 \longrightarrow \delta\mathcal{K} = [Q, Z]. \tag{39}$$

The variation $\delta\mathcal{K}$ is exact, since Q does not have cohomologies in V_1. We can write the variation of the solution to the anticommutativity equation, and after some algebra we get

$$\delta_\mathcal{K}\mathcal{F} = -\{\mathcal{D} - \mathcal{F}, \mathcal{F}_Z\}_s. \tag{40}$$

In (40), $\mathcal{F}_Z$ is obtained from the expression for $\mathcal{F}$ in terms of[2] $\mathcal{K}$ by the replacement of an insertion of $\mathcal{K}$ by Z. The variation of $\mathcal{F}$ in form (40) is an analogue of the gauge transformations in zero-curvature equation (23), because they retain this equation:

$$\{\mathcal{D} - \mathcal{F}, \mathcal{D} - \mathcal{F}\} = 0 \longrightarrow \{\mathcal{D} - \mathcal{F}, \delta\mathcal{F}\} = 0,$$
$$\{\mathcal{D} - \mathcal{F}, \delta_\mathcal{K}\mathcal{F}\} = \{\mathcal{D} - \mathcal{F}, \{\mathcal{D} - \mathcal{F}, \mathcal{F}_Z\}_s\} = 0. \tag{41}$$

The special property of the commutativity equation is that B_μ is invariant under variations of $\mathcal{K}$, as follows from (33) and (40). Really, $\mathcal{F}|_{\theta=0} = 0$ and $\mathcal{F}_Z|_{\theta=0} = 0$, so the variation term linear in θ is

$$\delta_\mathcal{K} B_\mu = \delta_\mathcal{K}\frac{\partial\mathcal{F}}{\partial\theta_\mu}\bigg|_{\theta=0} = 0. \tag{42}$$

In case of the anticommutativity equation, we have in general only two terms invariant under the variations of $\mathcal{K}$: $\mathcal{F}^{(1)}$ and $\mathcal{F}^{(2)}$.

Thus, we considered topological quantum mechanics as an example of topological field theory and showed that its special properties lead to numerous interesting relations for topological correlators in this theory. We proved that the generating function $\mathcal{F}$ for these correlators satisfies the anticommutativity equation $(\mathcal{D} - \mathcal{F})^2 = 0$. We showed that commutativity equation $[dB, dB] = 0$ could be considered as a special case of the anticommutativity equation.

The author is grateful to A. Morozov, A. Mironov, and A. Losev for fruitful discussions. The author is especially grateful to Kaiserslautern University for hospitality during the preparation of this work. This work was supported by the Russian Foundation for Basic Research (project no. 01-02-17682-a) and by the Volkswagen–Stiftung.

REFERENCES

1. E. Witten, Nucl. Phys. B **340**, 281 (1990).
2. E. Witten, Commun. Math. Phys. **121**, 351 (1989).
3. E. Witten, Commun. Math. Phys. **117**, 353 (1988).
4. E. Witten, Commun. Math. Phys. **118**, 411 (1988).
5. A. Losev, Preprint No. ITEP-TH-84/98, ITÉF (Inst. of Theoretical and Experimental Physics, Moscow, 1998); Preprint LPTHE-61/98 (1998).
6. A. Losev and Yu. Manin (in press).
7. A. Losev and I. Polyubin, Pis'ma Zh. Éksp. Teor. Fiz. **73**, 59 (2001) [JETP Lett. **73**, 53 (2001)].

[2] Schematically, $\mathcal{F} = \sum\Pi_0\Phi\mathcal{K}\Phi\mathcal{K}\ldots\Phi\mathcal{K}\Phi\Pi_0$.

JETP Letters, Vol. 76, No. 12, 2002, pp. 728–731. Translated from Pis'ma v Zhurnal Éksperimental'noĭ i Teoreticheskoĭ Fiziki, Vol. 76, No. 12, 2002, pp. 859–862.

Fractional Extensions of the Classical Isotropic Oscillator and the Kepler Problem

V. M. Eleonskiĭ, V. G. Korolev*, and N. E. Kulagin

Lukin Scientific Research Institute of Physical Problems, Zelenograd, Moscow, 124460 Russia

** e-mail: korolev@nonlin.msk.ru*

Received October 31, 2002

The class of fractional Hamiltonian systems that generalize the classical problem of the two-dimensional (2D) isotropic harmonic oscillator and the Kepler problem is considered. It is shown that, in the 4D space of structural parameters, the 2D isotropic harmonic oscillator can be extended along a line in such a way that the orbits remain closed and oscillations remain isochronous. Likewise, the Kepler problem can be extended along a line in such a way that the orbits remain closed for all finite motions and the third Kepler law remains valid. These curves lie on the 2D surfaces where any dynamical system is characterized by the same rotation number for all finite motions. © *2002 MAIK "Nauka/Interperiodica".*

PACS numbers: 45.20.Jj

It is known [1, 2] that, in the class of Hamiltonian systems $H = \frac{1}{2}|\mathbf{p}|^2 + U(|\mathbf{r}|)$ with two degrees of freedom, the orbits of all finite motions are closed in the two cases: in the Kepler problem ($U = -1/|\mathbf{r}|$) and in the isotropic harmonic oscillator. It is also known that, in the first case, this is due to a hidden symmetry (additional degeneracy) caused by the existence, in addition to the energy and angular momentum integrals, of a third integral of motion in the Kepler problem [3].

It is shown in this work that the class of Hamiltonians possessing these properties can be extended appreciably upon the transition to so-called fractional systems. Below, the following class of Hamiltonians is considered:

$$H = p^{\alpha_1} r^{\beta_1} + \sigma p^{\alpha_2} r^{\beta_2}, \tag{1}$$

where $r = |\mathbf{r}|$; $r = |\mathbf{p}|$; $\mathbf{r}, \mathbf{p} \in R^2$, and α_1, β_1, α_2, β_2, and σ are real parameters. This class includes, in particular, the Hamiltonian of a particle in the central field with potential $U \sim r^{\beta_2}$, $\alpha_1 = 2$, and $\beta_1 = \alpha_2 = 0$.

The dynamics of the Hamiltonian systems of class (1) were studied by us using the approach suggested in [4, 5]. We briefly describe its essence. Consider the Hamiltonian function of the form $H = H(p, r)$. By writing the vectors $\mathbf{p}$ and $\mathbf{r}$ in the polar coordinates (p, ψ) and (r, φ) and passing to the new angular variables $\Psi = \psi + \varphi$ and $\Phi = \psi - \varphi$, we obtain the following (noncanonical) equations of motion from the corresponding Hamiltonian equations:

$$\begin{aligned} \dot{r} &= \frac{\partial H}{\partial p}\cos\Phi, \quad \dot{p} = -\frac{\partial H}{\partial r}\cos\Phi, \\ \dot{\Phi} &= \left(\frac{1}{p}\frac{\partial H}{\partial r} - \frac{1}{r}\frac{\partial H}{\partial p}\right)\sin\Phi, \\ \dot{\Psi} &= \left(\frac{1}{p}\frac{\partial H}{\partial r} + \frac{1}{r}\frac{\partial H}{\partial p}\right)\sin\Phi, \end{aligned} \tag{2}$$

which have the first integrals

$$M = rp\sin\Phi = \text{const}, \quad E = H(p, r) = \text{const}. \tag{3}$$

Elimination of p and r from equations of motion (2) brings about the following system of equations for the angular variables (Ψ, Φ):

$$\begin{aligned} \ddot{\Phi} &= \cot\Phi\left\{2(\dot{\Phi})^2 + \frac{\theta_1 - \theta_2}{4D}(\zeta_1\dot{\Phi} - \theta_1\dot{\Psi})(\zeta_2\dot{\Phi} - \theta_2\dot{\Psi})\right\}, \\ \ddot{\Psi} &= \cot\Phi\left\{2\dot{\Phi}\dot{\Psi} + \frac{\zeta_1 - \zeta_2}{4D}(\zeta_1\dot{\Phi} - \theta_1\dot{\Psi})(\zeta_2\dot{\Phi} - \theta_2\dot{\Psi})\right\}, \end{aligned} \tag{4}$$

where $\zeta_i = \beta_i + \alpha_i$, $\theta_i = \beta_i - \alpha_i$ $(i = 1, 2)$, and $D = \beta_2\alpha_1 - \beta_1\alpha_2 \neq 0$.

Let us identify the configuration space of the dynamical system with the surface of a unit sphere (Φ and Ψ are the polar and azimuthal angles, respectively).

It should be emphasized that the arbitrary real exponents α_i and β_i in Hamiltonian (1) appear in Eqs. (4) only as coefficients, greatly simplifying the analysis of the problem.

The dynamical system (1) possesses a pair of integrals of motion:

$$I_1 = \frac{1}{D\sin^2\Phi}[(\theta_2-\theta_1)\dot\Psi-(\zeta_2-\zeta_1)\dot\Phi],$$
$$I_2 = (\sin\Phi)^{D-2(\theta_2-\theta_1)} \times\left[\frac{\theta_2\dot\Psi-\zeta_2\dot\Phi}{2D}\right]^{\theta_2}\left[\frac{\theta_1\dot\Psi-\zeta_1\dot\Phi}{-2\sigma D}\right]^{-\theta_1}, \quad (5)$$

with $I_1 = 2E/M$ and $I_2 = M^{D-(\theta_2-\theta_1)}$. It is assumed that $M \neq 0$ and that all negative values of power bases are excluded.

Excluding the angular velocity $\dot\Psi$ from the first equation in Eqs. (5), we arrive at the equations

$$\frac{\sin\Phi}{\sin\Phi_0}\left[1-\frac{1}{\nu_2}\frac{\Phi'}{\sin^2\Phi}\right]^{\nu_2}\left[1-\frac{1}{\nu_1}\frac{\Phi'}{\sin^2\Phi}\right]^{-\nu_1} = 1, \quad (6)$$

$$\Psi' = \frac{2}{D}\frac{\sin^2\Phi}{\nu_2-\nu_1}+\frac{\zeta_2-\zeta_1}{\nu_2-\nu_1}\Phi', \quad (7)$$

where $\Phi' = d\Phi/d\tau$, $\tau = (M/ED)t$, $\nu_1 = \theta_1/D$, $\nu_2 = \theta_2/D$, and the quantity $\sin^2\Phi_0 < 1$ is determined (for finite motions) by the relation

$$\frac{E^{\nu_2-\nu_1}}{M}\sin^2\Phi_0\left(\frac{\nu_2}{\nu_2-\nu_1}\right)^{\nu_2}\left(\frac{-\nu_1}{\sigma(\nu_2-\nu_1)}\right)^{-\nu_1} = 1. \quad (8)$$

One can see that

$$\Phi(\tau) = \Phi(\tau;\nu_1,\nu_2|E,M),$$
$$\Psi(\tau) = \Psi(\tau;\nu_1,\nu_2,D,\zeta_2-\zeta_1|E,M). \quad (9)$$

The general motion of a representative point on the sphere represents the rotation over the angle Ψ accompanied by the periodic oscillations of the polar angle Φ.

From Eq. (6), one can obtain the expression for the oscillation period T of the angle $\Phi(t)$ and the expression for the rotation number N (defined as the increment (divided by 2π) of the azimuthal angle Ψ during the period of polar angle Φ) of a trajectory on the sphere:

$$N = \frac{\sin\Phi_0}{\pi\nu_1\nu_2 D} \times\int_{z_-}^{z_+}\frac{(1-z/\nu_2)^{-1}(1-z/\nu_1)^{-1}dz}{\sqrt{(1-z/\nu_2)^{2\nu_2}(1-z/\nu_1)^{-2\nu_1}-\sin^2\Phi_0}}. \quad (10)$$

Here, $z_\pm$ ($z_- < z_+$) are the roots of the equation

$$\left(1-\frac{z}{\nu_2}\right)^{2\nu_2}\left(1-\frac{z}{\nu_1}\right)^{-2\nu_1} = \sin^2\Phi_0. \quad (11)$$

It is worth noting that, despite the fact that the function $\Psi(t)$ depends on the combination $\zeta_2-\zeta_1$, the rotation number N is independent of it. This signifies that, by fixing the values of three combinations $\theta_1 = \beta_1-\alpha_1$, $\theta_2 = \beta_2-\alpha_2$, and $D = \alpha_1\beta_2-\alpha_2\beta_1$ in the 4D space of the structural parameters $(\alpha_1,\beta_1,\alpha_2,\beta_2)$, we obtain straight lines

$$\alpha_1 = \alpha_1^0+k_1\gamma,\quad \beta_1 = \beta_1^0+k_1\gamma,$$
$$\alpha_2 = \alpha_2^0+k_2\gamma,\quad \beta_2 = \beta_2^0+k_2\gamma \quad (12)$$

($k_2/k_1 = (\beta_2-\alpha_2)/(\beta_1-\alpha_1)$ and γ is the parameter of straight line), along which the dependence of the rotation number N on the first integrals E and M is retained. For each straight line of type (12), there is a one-parameter family of Hamiltonian functions

$$H = p^{\alpha_1^0}r^{\beta_1^0}(rp)^{k_1\gamma}+\sigma p^{\alpha_2^0}r^{\beta_2^0}(rp)^{k_2\gamma}. \quad (13)$$

Fractional continuation of the Kepler problem. On the curve of type (12) passing through the point ($\alpha_1^0 = 2$, $\beta_1^0 = \alpha_2^0 = 0$, $\beta_2^0 = -1$) corresponding to the Kepler problem, one has $D = -2$, $\nu_1 = +1$, and $\nu_2 = 1/2$, with

$$\alpha_1 = 2+\gamma,\quad \beta_1 = \gamma,\quad \alpha_2 = \frac{\gamma}{2},\quad \beta_2 = -1+\frac{\gamma}{2}. \quad (14)$$

A pair of branches of the function $t = t(\Phi)$ is determined from Eq. (6):

$$\frac{\sigma^2(\sin\Phi_0)^3}{2M^3}(t-t_i) = \left\{\sin\Phi_0\cot\Phi\mp\arctan\frac{\cot\Phi}{\sqrt{\cot^2\Phi_0-\cot^2\Phi}}\right\}\Bigg|_{\Phi_i}^{\Phi}. \quad (15)$$

Integrating along the cycle $\Phi_0^- \longrightarrow \Phi_0^+ \longrightarrow \Phi_0^-$ ($0 < \Phi_0^- \le \pi/2 \le \Phi_0^+ < \pi$), one finds that the oscillation period of the function $\Phi(t)$ obeys the dependence $T(E) \propto (-E)^{-3/2}$, i.e., the third Kepler law holds at any γ. Integrating the equation

$$\frac{d\Psi}{d\Phi}+(\gamma-1) = \pm\frac{2\sin\Phi}{\sqrt{\sin^2\Phi-\sin^2\Phi_0}} \quad (16)$$

along the cycle, one finds that the increment of Ψ on the period of polar angle is 2π, irrespective of (E, M) and the parameter γ.

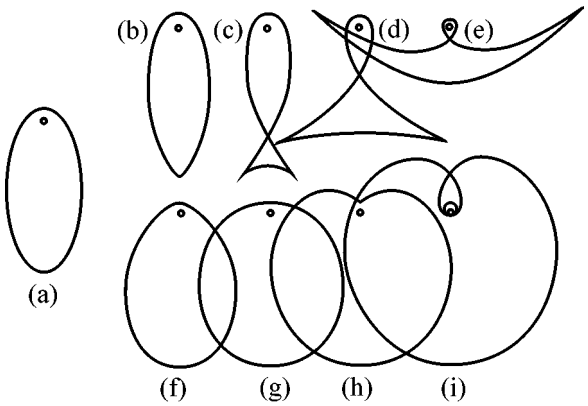

Typical transformation of orbits when moving along the one-parameter manifold (14): γ = (a) 0 (Kepler problem), (b) –0.15; (c) –0.45, (d) –1, (e) –2, (f) 0.45, (g) 1 (all orbits are circles with the center shifted from the origin of coordinates), (h) 2 (all orbits have the limaçon shape), and (i) 4.

Therefore, in the systems of one-parameter family

$$H = p^2(rp)^\gamma + \frac{\sigma}{r}(rp)^{\gamma/2}, \tag{17}$$

all finite orbits on the sphere are closed for any γ, so that the third Kepler law is valid. However, the orbit shapes depend on γ. One can readily verify that the conditions for closing orbits on the (r, φ) plane are also fulfilled for all γ values.

Finally, we present the formulas for the transformation of orbits on the (r, φ) plane upon varying γ:

$$r = 2\left(\frac{M}{\sin\varphi}\right)^\gamma r^0(\Phi), \quad r' = 2\left(\frac{M}{\sin\Phi}\right)^{\gamma'} r^0(\Phi),$$
$$\Phi = \Phi_0^- - 2\frac{\varphi' - \varphi}{\gamma' - \gamma}, \tag{18}$$

where (r, φ) and (r', φ') are the points on the orbits corresponding to the values of γ and γ' for the dynamical systems with Hamiltonian (17). In particular, these formulas can be used to derive the expression for the third integral of motion at $\gamma \neq 0$ using the known expression for the case of $\gamma = 0$ (i.e., the Kepler problem). This signifies that all dynamical systems of family (17) retain the hidden symmetry of the Kepler problem.

The orbit deformation on the (r, φ) plane upon varying the parameter γ is shown in the figure and confirmed by numerical calculations. The singularities appear on the orbits when (in certain intervals of γ values) $\dot{r} = 0$ and $\dot{\varphi} = 0$ (i.e., $\Phi = \pi/2$ and $\partial H/\partial p = 0$). Note that the reverse motion along the orbit ($\dot{\varphi}$ changes its sign) is not accompanied by a change in the direction of the vector of angular momentum; when moving back, the velocity vector is in opposition to the momentum vector.

Fractional continuation of the harmonic oscillator problem. Let us now consider the straight line of type (12) that passes through the point ($\alpha_1^0 = 2$, $\beta_1^0 = \alpha_2^0 = 0$, $\beta_2^0 = 2$). This corresponds to the harmonic oscillator problem. On this line, $D = 4$, $\nu_1 = -1/2$ and $\nu_2 = 1/2$; in this case,

$$\alpha_1 = 2 + \gamma, \quad \beta_1 = \gamma, \quad \alpha_2 = -\gamma, \quad \beta_2 = 2 - \gamma. \tag{19}$$

Equations (6) and (7) take the form

$$\dot{\Phi} = \pm 2\sigma^{1/2}\sin\Phi\sqrt{\frac{\sin^2\Phi}{\sin^2\Phi_0} \pm 1},$$
$$\dot{\Psi} = \frac{2E}{M}\sin^2\Phi - \gamma\dot{\Phi}.$$

Here, $\sin^2\Phi_0 = \sigma M^2/E^2$, and the differentiation is with respect to the initial independent variable t. Integrating the first of these equations (with a chosen lower limit of integration), we determine a pair of branches for the function $t = t(\Phi)$:

$$2\sigma^{1/2}(t - t_i) = \mp\arctan\frac{\cot\Phi}{\sqrt{\cot^2\Phi_0 - \cot^2\Phi}}\Bigg|_{\Phi_i}^{\Phi}. \tag{20}$$

Integrating along the cycle $\Phi_0^- \longrightarrow \Phi_0^+ \longrightarrow \Phi_0^-$, one finds that the period of function $\Phi(t)$ is $T = \sigma^{-1/2}$ and that it depends neither on (E, M) nor on the parameter γ. The azimuthal angle Ψ considered as a function of Φ is given by the expression

$$\Psi - \Psi_i = \mp\arcsin\frac{\cos\Phi}{|\cos\Phi_0|}\Bigg|_{\Phi_i}^{\Phi} - \gamma(\Phi - \Phi_i). \tag{21}$$

The increment of Ψ on the period T of polar angle equals π for any γ value; i.e., the deformation of orbits does not violate their closeness. In this case, $r(t + T, \gamma) = r(t, \gamma)$ and $\varphi(t + T, \gamma) = \varphi(t, \gamma) + \pi$. Thus, all dynamical systems with Hamiltonians

$$H = p^2(rp)^\gamma + \sigma r^2(rp)^{-\gamma} \tag{22}$$

are isochronous, and all orbits of finite motion in these systems are closed.

Two-parameter families. Under the condition $\theta_1 \neq \theta_2$, for each pair of real values (ν_1, ν_2), there is a 2D surface in the 4D space of structural parameters that is determined by two linear relations that connect θ_1, θ_2, and D with each other:

$$\theta_1 = \nu_1 D, \quad \theta_2 = \nu_2 D. \tag{23}$$

Let this pair of numbers (and, hence, the corresponding surface) be specified. For each fixed value of any of three quantities θ_1, θ_2, and D (for definiteness, let it be D), Eqs. (23) uniquely determine the values of the two other quantities; i.e., for each value of D there is a certain straight line of the form (12) lying at this surface. Thus, the surface of type (23) is stratified by straight lines (12).

Among such 2D surfaces, three are distinguished by their special properties and because they allow complete analysis of the respective dynamical systems. They are associated with the simplest commensurability types of the numbers ν_1 and ν_2. Specifically, these are the surface μ_1 ($\nu_1 = 1$, $\nu_2 = 1/2$), the surface μ_2 ($\nu_1 = -1/2$, $\nu_2 = 1/2$), and the surface μ_3 ($\nu_1 = 1/2$, $\nu_2 = 1$) that transforms to μ_1 by the obvious permutation $\alpha_1 \longleftrightarrow \alpha_2$ and $\beta_1 \longleftrightarrow \beta_2$ (the surface μ_2 transforms into itself upon the same permutation).

The surface μ_1 contains a point corresponding to the Kepler problem; it can be written in the form

$$\alpha_1 - 2\alpha_2 = 2, \quad \beta_1 - 2\beta_2 = 2 \tag{24}$$

and parameterized as

$$\begin{aligned} \alpha_1 &= -D + \gamma, \quad \beta_1 = \gamma, \\ \alpha_2 &= -D/2 + \gamma/2 - 1, \quad \beta_2 = \gamma/2 - 1. \end{aligned} \tag{25}$$

The Hamiltonian function corresponding to the arbitrary point with parameters $D \neq 0$ and γ at the surface μ_1 has the form

$$H = p^{-D}(rp)^{\gamma} - |\sigma| p^{-D/2}(rp)^{\gamma/2-1}. \tag{26}$$

A pair of branches of the function $t = t(\Phi)$ is determined from Eq. (15) by the change $\sigma^2/2M^3 \longrightarrow D\sigma^2/2M^3$. This signifies that $T \propto \frac{2}{D}(-E)^{-3/2}$.

Analysis shows that, for any dynamical system given by Eq. (26), all finite orbits at the surface μ_1 are characterized by the same rotation number $N = 2/|D|$. Therefore, by fixing D in Eq. (25), we obtain a straight line, which lies on the surface μ_1 and along which all systems are characterized by the same rotation number (common to all finite orbits). In particular, by setting $D = -2$, we obtain the above-considered line (14), which passes through the point corresponding to the Kepler problem. On the lines corresponding to the rational values of D, all finite orbits are closed, while on the lines corresponding to the irrational values of D, all finite orbits are open.

The surface μ_2 passes through the point corresponding to the harmonic oscillator problem; it is written in the form

$$\alpha_1 + \alpha_2 = 2, \quad \beta_1 + \beta_2 = 2 \tag{27}$$

and can be parameterized as

$$\begin{aligned} \alpha_1 &= D/2 + \gamma, \quad \beta_1 = -D/2 + 2 + \gamma, \\ \alpha_2 &= -D/2 + 2 - \gamma, \quad \beta_2 = D/2 - \gamma. \end{aligned} \tag{28}$$

It is also stratified by the straight lines along which the rotation number is conserved. Namely, the rotation number equals $2/|D|$ for all orbits of any system with the Hamiltonian function

$$H = \frac{p^{D/2}}{r^{-2+D/2}}(rp)^{\gamma} + |\sigma|\frac{r^{D/2}}{p^{-2+D/2}}(rp)^{-\gamma}. \tag{29}$$

In particular, by setting $D = 4$, we obtain the above-considered line (19), which passes through the point corresponding to the harmonic oscillator.

Numerical analysis indicates that the above-mentioned two-parameter families from the class given by Eq. (1) cover all systems for which the orbits of all finite motions in the system have the same rotation number.

In summary, the class of fractional Hamiltonian systems of type (1) is considered in this work. It is shown that, at $\sigma < 0$, there exists a one-parameter family of Hamiltonians of the form (1) that generalize the Kepler problem and for which all finite orbits are closed, so that the third Kepler law is valid. The orbits deform upon changing the parameter of the family. Nevertheless, all representatives of the family possess hidden symmetry (additional integral of motion).

At $\sigma > 0$, a one-parameter family of Hamiltonians of type (1) exists, which inherits from a 2D isotropic harmonic oscillator the closeness of orbits and the isochronism of oscillations (though nonlinear) for all $E > 0$. All representatives of this family also possess hidden symmetry.

Moreover, in each of the cases $\sigma < 0$ and $\sigma > 0$, the corresponding one-parameter family is a particular case of a certain two-parameter family of Hamiltonian functions. For each of them, all finite motions are characterized by the same rotation number. The orbits of all finite motions are closed if this number is rational and are otherwise open.

We are grateful to Prof. V.I. Yudovich for helpful discussion of the results.

REFERENCES

1. L. D. Landau and E. M. Lifshitz, *Course of Theoretical Physics*, Vol. 1: *Mechanics*, 4th ed. (Nauka, Moscow, 1988; Pergamon, New York, 1988).
2. V. I. Arnol'd, *Mathematical Methods of Classical Mechanics*, 3rd ed. (Nauka, Moscow, 1989; Springer, New York, 1989).
3. V. M. Alekseev, *Lectures on Celestial Mechanics* (RKhD, Izhevsk, 2000).
4. V. M. Eleonskiĭ, V. G. Korolev, and N. E. Kulagin, in *Abstracts of International Conference on Progress in Nonlinear Science* (Nizhni Novgorod, Russia, 2001).
5. V. M. Eleonskiĭ, V. G. Korolev, and N. E. Kulagin, in *Abstracts of International Conference on Nonlinear Problems of the Theory of Hydrodynamical Stability and Turbulence* (Moscow, 2002).

Translated by V. Sakun

JETP Letters, Vol. 76, No. 12, 2002, p. 732. Translated from Pis'ma v Zhurnal Éksperimental'noĭ i Teoreticheskoĭ Fiziki, Vol. 76, No. 12, 2002, p. 863.

In Memory of Our Contributors

PACS numbers: 01.60.+q

É.L. Nagaev, Magnetic Polarons (Ferrons) of Complicated Structure, JETP Lett. 74, 431 (2001).

Éduard Leonovich Nagaev, an outstanding theoretical physicist, distinguished specialist in the field of quantum theory of the solid state, Doctor of Physics and Mathematics, Winner of the State Premium of the USSR, Principal Research Scientist at the Institute of Radio Engineering and Electronics, Russian Academy of Sciences, died suddenly December 14, 2001. He was the author of pioneer research in the physics of magnetic semiconductors and the originator of the ferron concept. This concept (and, more generally, the idea of electronic phase layering in magnetic semiconductors and other materials) has found wide acceptance in the scientific community. This is, in particular, witnessed by the diploma for the discovery of "The Phenomenon of Heterophase Localization of Conduction Electrons in Semiconductors" (in collaboration with A.I. Larkin and D.E. Khmel'nitskiĭ). In recent years, this idea has proved to be particularly topical in view of the discovery of the colossal magnetoresistance effect in manganites. É.L. Nagaev accomplished a great deal of work on the physics of non-Heisenberg magnets, photoinduced magnetism, and the theory of small metallic particles. He made a tangible contribution to the theory of electronic processes in gases and electrolytes, polarons and excitons, the metal–insulator transition, superconductivity, and the isotope effect. Éduard Leonovich published more than 300 articles in journals (mostly without coauthors), of which 14 are reviews, and the monographs "Physics of Magnetic Semiconductors" (Nauka, Moscow, 1979; extended English edition Mir, Moscow, 1983) and "Magnets with Complex Exchange Interaction" (Nauka, Moscow, 1988). The book "Colossal Magnetoresistance and Phase Layering in Magnetic Semiconductors" (Imperial College, London, 2002) was published after his death. In JETP Letters, he published 25 works.

0021-3640/02/7612-0732$22.00